IRIS AperTO

UNIVERSITÀ DEGLI STUDI DI TORINO

AperTO - Archivio Istituzionale Open Access dell'Università di Torino

Rab11 activity and PtdIns(3)P turnover removes recycling cargo from endosomes

This is the author's manuscript

Original Citation:

Availability:

This version is available http://hdl.handle.net/2318/1692696 since 2019-02-15T17:28:09Z

Published version:

DOI:10.1038/s41589-018-0086-4

Terms of use:

Open Access

Anyone can freely access the full text of works made available as "Open Access". Works made available under a Creative Commons license can be used according to the terms and conditions of said license. Use of all other works requires consent of the right holder (author or publisher) if not exempted from copyright protection by the applicable law.

(Article begins on next page)

25 April 2024

Rab11 activity and PtdIns(3)*P* turnover removes recycling cargo from endosomes

Carlo Cosimo Campa[1,4*], Jean Piero Margaria[1*], Abhishek Derle[1,§], Marco Del Giudice[2,3,§], Maria Chiara De Santis[1], Luca Gozzelino[1], Francesca Copperi[1], Carla Bosia[2,3], Emilio Hirsch[1,4].

1. Department of Molecular Biotechnology and Health Sciences. Molecular Biotechnology Center, University of Turin, Via Nizza 52, 10126 Torino, Italy.
2. Department of Applied Science and Technology, Politecnico di Torino, C.so Duca degli Abruzzi 24, 10129, Torino, Italy.
3. Italian Institute for Genomic Medicine, via Nizza 52, 10126, Torino, Italy.
4. Corresponding authors:

Emilio Hirsch, PhD
Department of Molecular Biotechnology and Health Sciences.
Molecular Biotechnology Center (MBC),
University of Torino, Via Nizza 52, 10126 Torino, Italy
Tel. 0039 011 670 6425

Email: emilio.hirsch@unito.it

Carlo Cosimo Campa, PhD
Department of Molecular Biotechnology and Health Sciences.
Molecular Biotechnology Center (MBC),
University of Torino, Via Nizza 52, 10126 Torino, Italy
Tel. 0039 011 670 6425

Email: carlocosimo.campa@unito.it

*, §, These authors contributed equally to this work.

Abstract

Directional transport of recycling cargo from early endosomes (EE) to endocytic recycling compartment (ERC) relies on Phosphatidylinositol 3-phosphate (PtdIns(3)*P*) hydrolysis and activation of the small GTPase Rab11. However, how these events are coordinated is yet unclear. By using a novel genetically-encoded FRET biosensor for Rab11, we report that generation of endosomal PtdIns(3)*P* by the clathrin binding phosphoinositide 3-kinase Class 2 alpha (PI3K-C2α) controls the activation of Rab11. Active Rab11, in turn, prompts the recruitment of the phosphatidylinositol 3-phosphatase myotubularin 1 (MTM1), eventually enabling the release of recycling cargo from the EE and its delivery towards the ERC. Our findings thus define that delivery of recycling cargo towards the ERC requires spatial and sequential coupling of Rab11 activity with PtdIns(3)*P*-turnover.

Introduction

Intracellular trafficking of endocytosed molecules ensures the delivery of plasma membrane components and receptor-associated ligands to several cellular compartments. After internalization, such molecules can be either degraded or re-used by returning to the plasma membrane [1]. This recycling pathway restores the composition of plasma membrane and is mediated by vesicular carriers that transfer endocytosed material from peripherally located early endosomes (PE) to the endocytic recycling compartment (ERC), a juxtanuclear tubulovesicular compartment [2-4]. To be effective, this transport route requires regulated recruitment of molecular motors, membrane tethers, as well as lipid kinases and phosphatases in time and space[5-12]. Such engagement is partly accomplished by key determinants of functional identity of organelles including phosphatidylinositol 3-phosphate (PtdIns(3)*P*) and the small GTPase Rab11 [9, 13-16].

PtdIns(3)*P* is the major phosphoinositide residing on early endosomes where it serves as a membrane recognition site for the recruitment of proteins, thereby mediating endosomal fusion and maturation [17, 18]. PtdIns(3)*P* homeostasis is controlled by the coordinated action of lipid kinases and phosphatases. In particular, while phosphorylation of (PtdIns) to PtdIns(3)*P* requires members of the class II and class III phosphatidylinositol 3-kinase (PI3K) enzymes[10, 19-21], termination of PtdIns(3)*P* signaling relies on Myotubularins (MTMs), lipid phosphatases that convert PtdIns(3)*P* to (PtdIns) [22-25]. Although endosome maturation and recycling of endocytosed cargos requires control of PtdIns(3)*P* levels by the action of lipid kinases and phosphatases [8, 22, 26], the mechanism responsible for the regulated recruitment of these lipid metabolizing enzymes on endosomes remains largely unknown.

Extensive investigations demonstrated that members of the Rab protein family are coordinators of membrane domain formation and vesicle trafficking dynamics controlling the recruitment of endocytic regulators such as lipid kinases or phosphatases [27]. In particular, trafficking of endocytosed cargos toward the ERC is mediated by Rab11, a small GTPase enriched on ERC membranes and activated by signaling downstream of PI3K-C2α-derived PtdIns(3)*P* pool [9, 10, 20, 28]. In its active GTP-bound form, Rab11 mediates recycling and sorting of endocytosed membrane components through the ERC[12-14, 29]. However, whether the changes in Rab11 activity might determine the efficiency of membrane trafficking by controlling the phosphoinositide composition of endosomes is still unclear.

To monitor changes in Rab11 activity in living cells we developed a genetically-encoded FRET biosensor of active Rab11 named Activation Sensor Rab11 (AS-Rab11). Using this

biosensor, we demonstrated that the increase in Rab11 activity on PtdIns(3)P^+ peripheral endosomes is important to control the release of recycling cargoes, via a circuit involving sequential clathrin/PI3K-C2α-mediated PtdIns(3)*P* burst and subsequent Rab11/MTM1-dependent PtdIns(3)*P* hydrolysis.

Results

Development of a Rab11 FRET biosensor.

The activation cycle of Rab11 is essential to mediate the delivery of internalized plasma membrane components from PE to ERC [1, 30]. To monitor the spatial and temporal regulation of Rab11 nucleotide exchange in living cells, a genetically encoded fluorescence resonance energy transfer (FRET)-based probe, named Activation Sensor Rab11 (AS-Rab11), was developed (Figure 1a, Supplementary Figs.1a, b). The probe includes the C-terminal region of FIP3 binding active Rab11 only [31], a circular permuted version of a modified monomeric yellow fluorescent protein (mcpVenus), a proteinase K-sensitive linker, a monomeric cyan fluorescent protein (mECFP) and human Rab11a (Figure 1a). In this probe design, an increase in GTP-loading of Rab11 promotes the binding of the C-terminal region of FIP3 to Rab11a, thus modifying the orientation of the two fluorophores and thereby increasing FRET which is represented by the 525 nm/475 nm (FRET/CFP) emission ratio [32, 33](Figure 1a). The positioning of Rab11 at the C-terminal end of AS-Rab11 allows correct functioning of the Rab11 C-terminal sequences required for membrane insertion (Figure 1a).

To validate the efficiency of the biosensor energy transfer in the presence of either GDP or GTP, the fluorescence emission profiles of AS-Rab11 were monitored using a fluorometric assay (*see Materials and Methods*). In comparison with the wild type form, constitutively active mutant versions of Rab11 lacking GTPase activity (AS-Rab11^{Q70L} and AS-Rab11^{S20V}) showed decreased fluorescence emission intensity at 475 nm and a concomitant increase at 525nm (Figure 1b, Supplementary Fig. 1c red line). Consequently, the FRET/CFP ratio of AS-Rab11^{Q70L} and AS-Rab11^{S20V} were found significantly higher than the wild-type and the nucleotide-free (AS-Rab11^{N124I}) forms (Figure 1b, Supplementary Fig. 1c). In contrast, a dominant negative version of this biosensor (AS-Rab11^{S25N}, Supplementary Fig. 1c blue line) displayed 475 nm and associated 525nm emission higher and lower than the control, respectively (Figure 1b, Supplementary Fig. 1c cyan line, Supplementary Fig. 1d). A similar observation was made after proteinase-K treatment of AS-Rab11 wild-type (Supplementary Fig. 1c black line) that induced the cleavage of the amino acidic linker connecting the two fluorophores required to promote the energy transfer. Consequently, both AS-Rab11^{S25N} and proteinase-K-treated AS-Rab11^{wt} showed decreased FRET emission ratio (Figure 1b, Supplementary Fig. 1c blue and black lines), and similarly to a Rab11-GTP binding mutant (AS-Rab11$^{RBD\ mutant}$) (Figure 1b). In line with these results, increased FRET emission ratio and Rab11-GTP content were detected after co-expression of AS-Rab11^{wt} with SH3BP5, a Rab11-GEF [34] (Figures 1b, Supplementary Fig. 1e). On the contrary, co-expression of

TBC1D9B, a Rab11-GAP [35] decreased FRET emission ratio and Rab11-GTP content in cells (Figures 1b, Supplementary Fig. 1e). A similar emission was obtained by co-expression of RabGDI, a Rab11 dissociation inhibitor [36], and was reverted by the use of a GDI-insensitive biosensor mutant (AS-Rab11^{N206X})(Figure 1b). This regulation was found specific, as co-expression of AS-Rab11^{wt} with either Rac1 or Rab5 GEFs and GAPs had no effect on biosensor response (Figure 1b). Next, AS-Rab11 binding to guanine nucleotides was assessed by thin layer chromatography. Equal amounts of GDP and GTP associated with the wild-type biosensor form, whereas either GTP or GDP bound the constitutively active (Q70L) or the dominant negative (S25N) biosensor forms, respectively (Supplementary Fig. 1f). At the same time, AS-Rab11 was able to bind and replace GDP with GTP similarly to Rab11 (Supplementary Fig. 1g). The biosensor was found to interact with recombinant FLAG-RabGDI, FLAG-SH3BP5, and FLAG-TBC1D9B (Supplementary Figs. 2a-c). Whereas AS-Rab11$^{RBD\ mutant}$ interacted with endogenous FIP2 and FIP4, AS-Rab11^{WT} did not, indicating that the probe in its active conformation is not able to compete for endogenous targets (Supplementary Fig. 2d). Finally, As-Rab11 localized with markers of early and recycling endosomes but was absent from cis-Golgi and late endosome structures (Supplementary Figs. 3a-e), thus showing a pattern consistent with the functions of unmodified, endogenous Rab11.

Increased FRET emission ratio was detected both on tubulovesicular structures situated in the proximity of the nucleus and on small membrane-bound organelles positioned at the cell periphery (Figures 1c, d). To exclude the possibility that such high FRET efficiency was caused by random probe accumulation, a correlation plot of the sensitized FRET (i.e. the measure of FRET efficiency corrected for excitation and emission crosstalk) versus the CFP intensities was generated. Sensitized FRET was higher in endosomes than in cytosol (Figure 1e), as indicated by the 2 different slopes of the regression line that correlates the sensitized FRET and the CFP intensities measured in endosomes and cytosol, respectively. Moreover, to assess the spatial distribution of active Rab11 in cells, the FRET/CFP ratio of structures was measured as a function of the distance from the nucleus and FRET emission ratio appeared significantly higher on the ERC than on PE (Figure 1f).

Overall, these results demonstrate that this biosensor can monitor the nucleotide binding status of Rab11 and that active Rab11 is spatially restricted in both peripheral and juxtanuclear endosomal structures.

Activated-Rab11 labels PtdIns(3)P$^+$ endosomes.

To examine the subcellular distribution and the identity of membrane-bound structures displaying active Rab11, AS-Rab11-expressing cells were analyzed by confocal microscopy after

the internalization of fluorescent transferrin (Tf-647), an early-recycling endosome marker [16]. In line with previous studies [13, 14], perinuclear accumulation of active Rab11 (Figure 2a left panel, pseudocolor map) and Tf-647 (Figure 2a left panel, gray scale) was observed. In addition, enlargement of the peri-plasmalemmal region showed overlap between the highest FRET signal (Figure 2a right panel, red line) and Tf-647 (Figure 2a right panel, black line). Accordingly, two-dimensional representation of pixel intensities (Figure 2a right panel, line intensity profile) along a line starting from the nucleus and reaching the plasma membrane (Figure 2a left panel, white line) showed almost perfect overlap between FRET ratio (Figure 2a righ panel, red line) and Tf-647 (Figure 2a right panel, black line) signals in both the perinuclear and peripheral region. In further agreement, analysis of colocalization, as determined by Pearson's coefficient, showed high correlation between FRET ratio and Tf-647 positivity both in the ERC and PE (Figure 2a right panel), indicating that active Rab11 is equally distributed in perinuclear and peripheral Tf-positive compartments.

To gain insight into the localization of active Rab11, early and recycling endosome specific markers were similarly studied by analyzing a red fluorescent tagged versions of either Rab4, Rab5 or the PtdIns(3)*P* probe mCherry-FYVE2X. Identical distribution and strong colocalization were observed by fine mapping of active-Rab11 and mRFP-Rab4-positive structures, in pseudocolor and grayscale, respectively (Figure 2b). Conversely, endosomal membranes labelled by mRFP-Rab5 colocalized with active Rab11 at the cell periphery but not at the perinuclear recycling compartment (Figure 2c). Similarly, active-Rab11 strongly co-localized with the early endosome marker PtdIns(3)*P*, as detected with the mCherry-FYVE2X probe, on peripheral but not on perinuclear membrane-bound structures (Figure 2d). These results indicate that PEs, in which active Rab11 colocalized with PtdIns(3)*P*, correspond to early endosomes.

Exit from endosome relies on Rab11 and PtdIns(3)P

To examine the relationship between Rab11, PtdIns(3)*P* and recycling cargo in peripheral endosomes, the localization of Rab11 and Transferrin receptor (TfR) on PtdIns(3)*P*-positive structures was monitored during the continuous uptake of Tf. Confocal microscopy analysis revealed a frequent growth of tubular $Rab11^{+}$/mCherry-TfR^{+} structures from PEs (Figure 3a). Furthermore, Tf uptake increased Rab11 activity (Supplementary Figs. 4a, b) and expression of a Rab11 dominant negative form inhibited Tf recycling and promoted its accumulation (Supplementary Figs. 4c-e), thus indicating that removal of recycling cargo from endosomes requires Rab11 activation. In agreement, increased FRET/CFP signal on the nascent vesicle began 5 seconds before fission, concomitantly with a PtdIns(3)*P* burst, and reached maximal signal at the

time of fission (Figures 3b, c, Supplementary Figs. 4f-h). Such activation kinetics did not rely on biosensor abundance as both temporal assessment and titration of AS-Rab11 level on endosomes showed robust and coherent biosensor response at various probe expression levels (Figure 3c grey line, Supplementary Figs. 4i). Unexpectedly, on the nascent recycling structure, Rab11 activation was initially preceded by the increase of PtdIns(3)*P*-levels but was later followed by a PtdIns(3)*P* decrease, starting at the time of fission (Figures 3b, c, Supplementary Figs. 4f-h). These results show that, on peripheral endosomes, PtdIns(3)*P* peaks concomitantly with Rab11 activation and declines with the fission of recycling cargo-containing vesicles.

To gain insight into this process, COS-7 cells expressing perinuclear localized AS-Rab11 were bleached to avoid contaminating signals from the ERC region and movement of active $Rab11^+$ vesicles was analyzed after Tf addition (Figure 3d). $Rab11^+$ vesicles followed long-range linear movements and then eventually collapsed into ERC membranes (Figure 3d), thus indicating that juxtanuclear AS-Rab11-positive structures derived in part from peripheral endosomes. Accordingly, AS-Rab11-positive endosomal structures accumulated in the perinuclear region during the continuous uptake of Tf and resulted in a steady state after 15 minutes (Supplementary Figs. 5a-e). By interfering with microtubule polymerization using a treatment with Nocodazole, vesicles carrying an active Rab11 failed to appear as a linear series of dots over time (Supplementary Fig. 5f). This indicated that disruption of microtubule-dependent transport abolished long-range movements of AS-Rab11-positive membranes without compromising Tf accumulation (Supplementary Figs. 5f-h). Consistently, displacement of endocytic structures, as well as Rab11 activation were decreased upon Nocodazole treatment (Figures 3e, f). These data suggested that minus end-directed microtubule motor transport is required for endocytic structure movement. To test this hypothesis, acute inactivation of retrograde transport using Ciliobrevin D, a Dynein inhibitor [37], was performed. Ciliobrevin D treatment decreased long-range retrograde motion of active $Rab11^+$ vesicles and had a minor impact on vesicle linear movement/displacement (Figures 3e, g, h) consistently with multiple Rab11/microtubule-dependent trafficking routes [38]. Finally, both Nocodazole and Ciliobrevin D treatments decreased juxtanuclear accumulation of endocytosed transferrin (Figures 3i, j).

Overall, these data indicate that transferrin receptor is removed from PEs and transported to the ERC through a local increase of PtdIns(3)*P*, the activation of Rab11, the hydrolysis of PtdIns(3)*P*, and eventually the dynein-mediated vesicular transport.

PI3K-C2α controls Rab11 activity on PtdIns(3)P$^+$ endosomes

In early endosomes, PtdIns(3)*P* is mainly produced by Class III PI3K. However, a small but significant amount of PtdIns(3)*P,* ranging up to 20%, derives from Class II PI3Ks [39] and is putatively required for Rab11 activation [9, 10]. To further determine whether the activation of Rab11 preferentially depended on either Class II or III PI3K, modulation of the AS-Rab11 probe was studied after either PI3K-C2α or Vps34 knock-down or Vps34 inhibition (Supplementary Figs. 6a-c). As expected, knock-down of PI3K-C2α induced a 20% loss of PtdIns(3)*P* as well as a 50% drop in Rab11 activity (Figures 4a, b). On the contrary, knock-down or inhibition of Vps34 by VPS34-IN1 decreased PtdIns(3)*P* cell content by 80% but failed to significantly reduce the levels of active Rab11 (Figures 4a, b). This highlights the distinct role of PI3K-C2α in controlling Rab11 activity in PE. In addition, PI3K-C2α localization during cargo release from PtdIns(3)*P*$^+$ structures was imaged. GFP-PI3K-C2α co-localized with mCherry-FYVE2X during the fission of mECFP-Rab11 positive structures (Figures 4c, Supplementary Figs. 6d-f), while it was undetected in the newly formed mECFP-Rab11$^+$/mCherry-TfR$^+$ membranes (Supplementary Figs. 6e-g). Interestingly, such PI3K-C2α localization strictly depended on its N-terminal Clathrin binding domain [40], as loss of this domain [41] resulted in a diffuse cytosolic distribution around the PE (Figure 4d).

Number, displacement and direction of Rab11-positive vesicles leaving PEs were analyzed in PI3K-C2α-knock-down cells to further characterize the role of PI3K-C2α in the control of Rab11-mediated intracellular trafficking. Reduction of PI3K-C2α abundance as well as the expression of GFP-Rab11^{S25N} lowered the number of Rab11$^+$ vesicles emerging from PEs (Figure 4e). In further support, increased residence time of Rab11 at the PEs was observed in both PI3K-C2α-KD and Rab11^{S25N} expressing cells (Figure 4f). On the contrary, pharmacological inhibition of Vps34 did not alter either the number of fission events or the residence time of Rab11 on PEs (Figures 4e, f), strengthening the idea that Vps34 and PI3K-C2α present non-redundant functions during the endocytic recycling of transferrin.

Next, to further confirm this evidence, quantitation and localization of labelled Tf were performed. PI3K-C2α-KD and GFP-Rab11^{S25N}-expressing cells displayed increased Tf accumulation and decreased Tf perinuclear storage, which was not affected by either inhibition or RNAi-mediated suppression of Vps34 (Figures 4g, h, Supplementary Figs. 6c, h). Such transferrin recycling delay did not depend on the efficiency of molecular motors, as similar distribution of linearity and vesicle speed between GFP-Rab11^{S25N} expressing cells, PI3K-C2α-KD and controls were measured by tracking of individual Rab11$^+$ vesicles (Supplementary Figs. 6i, j). This Tf delivery defect in PI3K-C2α-KD cells was rescued by expression of a wild-type (PI3K-C2α^{WT}) or a

PI3P-only producing PI3K-C2α form (PI3K-C2α^{CIII}) (Figure 4i). On the contrary, expression of a kinase inactive mutant (PI3K-C2α^{R1251P}) did not restore juxtanuclear Tf localization (Figure 4i), thus demonstrating that Tf delivery to perinuclear endosomes is controlled by the PI3K-C2α-dependent PI3P production. In line with these results, silencing of PI3K-C2α led to the intracellular entrapment of Tf (Supplementary Fig. 6k).

Altogether, these results indicated that removal of recycling cargo from early endosomes requires PI3K-C2α-mediated PI3P production, necessary for Rab11 activation. Nonetheless, PtdIns(3)*P* decreased prior fission and disappeared from the detached Rab11^{+} vesicle, suggesting that removal of recycling cargo from endosomes depends on PtdIns(3)*P* hydrolysis.

The PtdIns(3)P phosphatase MTM1 is a Rab11 effector

In order to identify the PtdIns(3)*P* phosphatase that connects the increase in Rab11 activity with the concomitant decrease of PtdIns(3)*P*, pull-down of potential PtdIns(3)*P* phosphatases working as Rab11 effectors was performed. Five different PtdIns(3)*P* phosphatases, members of the Myotubularin protein family, were tested using immobilized Glutathione S-transferase (GST)-Rab11 as a probe. Among them, MTM1 was found to preferentially bind Rab11:GTP-γS rather than Rab11:GDP (Figure 5a). On the contrary, no interactions were detected for MTMR2, MTMR4, MTMR6, MTMR9 (Figure 5a). Remarkably, MTM1 was isolated from total cell extracts by pull-down of Rab11-GTP using a recombinant Rab11-GTP interacting protein (GST-RBD11) as a probe [9] (Figure 5b), and by immunoprecipitation of endogenous Rab11 (Supplementary Fig. 7a), thus indicating that Rab11 is associated with MTM1 *in vivo*. In further agreement, an *in vitro* binding assay using purified GST-Rab11 and His-Flag-MTM1 showed preferential binding of recombinant MTM1 with Rab11:GTP-γS compared to Rab11:GDP or other Rabs (Figures 5c, Supplementary Fig. 7b). RNA-interference mediated downregulation of MTM1 (MTM1-KD) (Supplementary Fig. 7c) significantly increased PtdIns(3)*P* levels as well as Rab11 activity (Figures 5d, e). In MTM1-KD cells, additional silencing of PI3K-C2α but not of Vps34 reduced Rab11 activation (Figure 5e). These results indicated that active Rab11 is associated with the PtdIns(3)*P* phosphatase MTM1 which actively dephosphorylates the PtdIns(3)*P* present on the structures directed towards the ERC. In agreement with this view, confocal microscopy analysis showed that Rab11 and MTM1 colocalized both in PE and ERC membranes as well as in TfR^{+} vesicles (Figures 5f, g, Supplementary Fig. 7d). In line with these results, Rab11 silencing blocked perinuclear and peripheral MTM1 localization (Supplementary Fig. 7e).

To further characterize the impact of MTM1 in the control of Rab11-mediated intracellular trafficking, $Rab11^{+}$ vesicles detaching from PEs were analyzed after RNAi-mediated downregulation of MTM1 (MTM1-KD). Loss of MTM1 as well as expression of GFP-$Rab11^{S25N}$ decreased the number of Rab11 positive fission events from PEs (Figure 5h), without affecting vesicle speed (Supplementary Fig. 7f). Furthermore, the residence time of Rab11 positive structures on PEs increased in both conditions (Figure 5i). Therefore, either impaired activation of Rab11 or lack of the phosphatase activity delayed fission. In agreement, MTM1-KD and GFP-$Rab11^{S25N}$-expressing cells displayed increased Tf content and decreased perinuclear accumulation of the recycling cargo (Figures 5j, k, Supplementary Fig. 7g). To identify the lipid kinase that antagonizes MTM1 activity, the rescue of Tf uptake and Tf accumulation of the recycling cargo at the ERC were performed. Acute perturbation of PtdIns(3)*P* synthesis by Vps34 inhibition partially restored Tf accumulation and perinuclear storage in MTM1-KD cells (Figures 5j, k) without affecting the increase in Rab11 activation due to MTM1 loss (Figure 5e). In agreement, Rab11-mediated fission events appeared more frequent in MTM1-KD/VPS34-IN1 than in MTM1-KD cells (Figure 5h), thus indicating that fission requires a significant reduction of PtdIns(3)*P*. In the absence of MTM1, knock-down of either PI3K-C2α alone or in combination with Vps34 inhibition led to decreased Rab11 activity. Conversely, in the absence of MTM1, Vps34 inhibition alone was not able to restore increased Rab11 activity (Figure 5e). Therefore, PI3K-C2α is the main kinase driving PtdIns(3)*P* production required for Rab11 activation, consequent fission and Tf recycling (Figure 5h, j, k).

Taken together, these results show that removal of recycling cargo from peripheral endosomes depends on subsequent PI3K-C2α-mediated PtdIns(3)*P* production, Rab11 activation and MTM1-dependent PtdIns(3)*P* destruction, leading to fission of vesicles and their eventual dynein-mediated transport to the ERC.

Discussion

Removal of recycling cargo from peripheral PtdIns(3)P^+ endosome requires PtdIns(3)*P* hydrolysis and the activation of the small GTPase Rab11. However, whether these events are linked is unknown. Therefore, a genetically-encoded FRET biosensor for Rab11 was generated to detect spatial and temporal variations of Rab11 activity in endosomes. This biosensor named AS-Rab11 was proven to be effective into limited diffusional space, such as in membrane and vesicular compartments and its activity was found to depend on both positive and negative Rab11 regulators, such as Rab11 GEF, GAP and GDI [34-36]. Using AS-Rab11, we revealed that: (I) Rab11 activation is initiated on PtdIns(3)*P*-positive membranes where sorting of recycling cargo occurs; (II) Rab11 activation level determines the release rate of membranes destined to the ERC; and (III) such release required MTM1, a PtdIns(3)*P* phosphatase, which was found to interact with active Rab11. These results establish that removal of recycling cargo from peripheral PtdIns(3)P^+ endosome requires coupling of Rab11 activity and PtdIns(3)*P* turnover (Figure 6).

Extensive time lapse analyses and biochemical experiments revealed enrichment of active-Rab11 on juxtanuclear positioned ERC and peripheral PtdIns(3)P^+ endocytic structures. In addition, they evidenced a critical role of activated Rab11 in the release of Transferrin receptors (TfR) from PtdIns(3)P^+ membranes. Given that PtdIns(3)*P* is a bona-fide marker [18] of EE, a compartment where recycling cargoes are sorted and directed toward the ERC or plasma membrane [14, 28], our data suggest that Rab11 activation is initiated on EE membranes where sorting of recycling cargoes occurs. In agreement, the direct visualization of active Rab11 patches localizing with TfR on PtdIns(3)P^+ membranes corroborate these evidences. Our experiments show that membranes decorated by active Rab11 are not maintained indefinitely on PtdIns(3)P^+ structures but are delivered from peripheral to juxtanuclear recycling compartment. These observations define that, differently from active Rab5 that mediates the expansion of Rab5 domain on early endosomes, active Rab11 critically affects cargo flow by recruiting the protein machinery involved in vesicle transport. In line with this view, our results evidenced that active Rab11 vesicles detaching from peripheral endosomes accumulate on ERC membranes in a dynein-dependent manner.

Our observations extend the previous identification of PI3K-C2α as a key controller of Rab11 activation on endosomes [9] and define that localization of PI3K-C2α on endosomes strictly depends on its clathrin binding domain [20, 40]. Notably, depletion of PI3K-C2α delays the kinetic of vesicle release from PtdIns(3)P^+ structure where TfR sorting takes place [1], thus linking the role of PI3K-C2α to endosomal sorting. Accordingly, depletion of PI3K-C2α, as well as loss of its catalytic

activity, decreases both activity and fission of Rab11-positive vesicles from PtdIns(3)P^+ structures, thereby mimicking the phenotype observed in cells expressing dominant negative Rab11.

In light of the highly dynamic Rab11 activation on PtdIns(3)P^+ structures, and the distinct phosphoinositide composition of EE and the perinuclear recycling compartment [42], a phosphoinositide conversion can be expected between these two Rab11 positive membrane domains. Our data demonstrated that this transition is controlled by MTM1, which was found to interact with active Rab11. MTM1 was shown to antagonize the Class II and Class III derived PtdIns(3)*P* pools in *D. melanogaster* and *C. elegans* and was demonstrated to be essential in the exit of cargos from PtdIns(3)*P* endosomes [8, 26]. Accordingly, $MTM1^+$/$Rab11^+$ vesicles were observed during removal of recycling cargo from PtdIns(3)*P* compartment, thus indicating that active Rab11 provides a signal to control MTM1 localization. Given that recycling vesicles require dynein to reach the ERC, removal of PI3P can be explained by the fact that the presence of this lipid, a well-known activator of centrifugal kinesin-mediated transport[43], might disturb this centripetal trafficking.

The development and application of AS-Rab11 to quantitatively analyze Rab11 activity in living cells allowed to dissect and analyze the initial step of the PtdIns conversion mechanism [42] required for the exit of recycling cargo from endosomes. Our data indicate that PI3K-C2α provides a spatially localized and temporally controlled PtdIns(3)*P* pool sufficient to activate Rab11 on early endosomes, allowing establishment and maintenance of receptor recycling towards the ERC. Activation of Rab11 eventually contributes to the recruitment of MTM1 and the ensuing reduction of PtdIns(3)*P* level on membranes destined to the perinuclear endosome.

Acknowledgements:

We are grateful to Cecilia Bucci from University of Salento, Ken Sato from University of Gunma, Gerard Apodaca from University of Pittsburgh, Matteo Bonazzi from University of Montpellier, Jocelyn Laporte from Institut de Génétique et de Biologie Moléculaire et Cellulaire (IGBMC), Letizia Lanzetti from Candiolo Cancer Institute and Sara Sigismund, Giorgio Scita and Andrea Palamidessi from Fondazione Istituto FIRC di Oncologia Molecolare (IFOM) for providing reagents. We are grateful to Marta Gai from University of Turin for providing technical support in confocal microscopy.

Author Contribution:

C.C.C., J.P.M., and E.H. conceived and designed the experiments. C.C.C., M.D.S, L.G. and F.C perform in vitro experiments and analyzed the data, J.P.M., C.C.C., A.D, perform in vitro experiments and analyzed the data, M.D.G and C.B. analyzed imaging data, C.C.C. and E.H. wrote the manuscript. All authors contributed to data interpretation. All authors reviewed the paper and provided comments.

Conflict of interest:

EH is a co-founder of Kither Biotech, a company involved in the development of PI3K inhibitors. The other authors declare that the research was conducted in the absence of any commercial and financial relationships that could be construed as a competing financial of interest.

Funding statement

This work was supported by “Futuro e Ricerca 2010” (RBFR10HP97_004). C.C.C. was supported by a FIRC (Fondazione italiana ricerca sul cancro) research fellowship. J.P.M was supported by a UIF (Università Italo-Francese) co-tutele Phd programme.

References:

1. Maxfield, F.R. & McGraw, T.E. Endocytic recycling. *Nat Rev Mol Cell Biol* **5**, 121-132 (2004).
2. Cullen, P.J. Endosomal sorting and signalling: an emerging role for sorting nexins. *Nat Rev Mol Cell Biol* **9**, 574-582 (2008).
3. Mellman, I. & Nelson, W.J. Coordinated protein sorting, targeting and distribution in polarized cells. *Nat Rev Mol Cell Biol* **9**, 833-845 (2008).
4. Jovic, M., Sharma, M., Rahajeng, J. & Caplan, S. The early endosome: a busy sorting station for proteins at the crossroads. *Histol Histopathol* **25**, 99-112 (2010).
5. Takahashi, S. et al. Rab11 regulates exocytosis of recycling vesicles at the plasma membrane. *J Cell Sci* **125**, 4049-4057 (2012).
6. Winter, J.F. et al. Caenorhabditis elegans screen reveals role of PAR-5 in RAB-11-recycling endosome positioning and apicobasal cell polarity. *Nat Cell Biol* **14**, 666-676 (2012).
7. Jovic, M. et al. Endosomal sorting of VAMP3 is regulated by PI4K2A. *J Cell Sci* **127**, 3745-3756 (2014).
8. Ketel, K. et al. A phosphoinositide conversion mechanism for exit from endosomes. *Nature* **529**, 408-412 (2016).
9. Franco, I. et al. PI3K class II alpha controls spatially restricted endosomal PtdIns3P and Rab11 activation to promote primary cilium function. *Dev Cell* **28**, 647-658 (2014).
10. Franco, I. et al. Phosphoinositide 3-Kinase-C2alpha Regulates Polycystin-2 Ciliary Entry and Protects against Kidney Cyst Formation. *J Am Soc Nephrol* **27**, 1135-1144 (2016).
11. Horgan, C.P., Hanscom, S.R., Jolly, R.S., Futter, C.E. & McCaffrey, M.W. Rab11-FIP3 binds dynein light intermediate chain 2 and its overexpression fragments the Golgi complex. *Biochem Biophys Res Commun* **394**, 387-392 (2010).
12. Horgan, C.P., Hanscom, S.R., Jolly, R.S., Futter, C.E. & McCaffrey, M.W. Rab11-FIP3 links the Rab11 GTPase and cytoplasmic dynein to mediate transport to the endosomal-recycling compartment. *J Cell Sci* **123**, 181-191 (2010).
13. Ren, M. et al. Hydrolysis of GTP on rab11 is required for the direct delivery of transferrin from the pericentriolar recycling compartment to the cell surface but not from sorting endosomes. *Proc Natl Acad Sci U S A* **95**, 6187-6192 (1998).
14. Ullrich, O., Reinsch, S., Urbe, S., Zerial, M. & Parton, R.G. Rab11 regulates recycling through the pericentriolar recycling endosome. *J Cell Biol* **135**, 913-924 (1996).
15. Traer, C.J. et al. SNX4 coordinates endosomal sorting of TfnR with dynein-mediated transport into the endocytic recycling compartment. *Nat Cell Biol* **9**, 1370-1380 (2007).
16. Sonnichsen, B., De Renzis, S., Nielsen, E., Rietdorf, J. & Zerial, M. Distinct membrane domains on endosomes in the recycling pathway visualized by multicolor imaging of Rab4, Rab5, and Rab11. *J Cell Biol* **149**, 901-914 (2000).
17. Balla, T. Phosphoinositides: tiny lipids with giant impact on cell regulation. *Physiol Rev* **93**, 1019-1137 (2013).
18. Simonsen, A. et al. EEA1 links PI(3)K function to Rab5 regulation of endosome fusion. *Nature* **394**, 494-498 (1998).
19. Braccini, L. et al. PI3K-C2gamma is a Rab5 effector selectively controlling endosomal Akt2 activation downstream of insulin signalling. *Nat Commun* **6**, 7400 (2015).
20. Campa, C.C., Franco, I. & Hirsch, E. PI3K-C2alpha: One enzyme for two products coupling vesicle trafficking and signal transduction. *FEBS Lett* **589**, 1552-1558 (2015).
21. Backer, J.M. The regulation and function of Class III PI3Ks: novel roles for Vps34. *Biochem J* **410**, 1-17 (2008).

22. Jean, S., Cox, S., Schmidt, E.J., Robinson, F.L. & Kiger, A. Sbf/MTMR13 coordinates PI(3)P and Rab21 regulation in endocytic control of cellular remodeling. *Mol Biol Cell* **23**, 2723-2740 (2012).
23. Cao, C., Backer, J.M., Laporte, J., Bedrick, E.J. & Wandinger-Ness, A. Sequential actions of myotubularin lipid phosphatases regulate endosomal PI(3)P and growth factor receptor trafficking. *Mol Biol Cell* **19**, 3334-3346 (2008).
24. Cao, C., Laporte, J., Backer, J.M., Wandinger-Ness, A. & Stein, M.P. Myotubularin lipid phosphatase binds the hVPS15/hVPS34 lipid kinase complex on endosomes. *Traffic* **8**, 1052-1067 (2007).
25. Hnia, K., Vaccari, I., Bolino, A. & Laporte, J. Myotubularin phosphoinositide phosphatases: cellular functions and disease pathophysiology. *Trends Mol Med* **18**, 317-327 (2012).
26. Velichkova, M. et al. Drosophila Mtm and class II PI3K coregulate a PI(3)P pool with cortical and endolysosomal functions. *J Cell Biol* **190**, 407-425 (2010).
27. Wandinger-Ness, A. & Zerial, M. Rab proteins and the compartmentalization of the endosomal system. *Cold Spring Harb Perspect Biol* **6**, a022616 (2014).
28. Campa, C.C. & Hirsch, E. Rab11 and phosphoinositides: A synergy of signal transducers in the control of vesicular trafficking. *Adv Biol Regul* **63**, 132-139 (2017).
29. Lu, Q. et al. Early steps in primary cilium assembly require EHD1/EHD3-dependent ciliary vesicle formation. *Nat Cell Biol* **17**, 531 (2015).
30. Welz, T., Wellbourne-Wood, J. & Kerkhoff, E. Orchestration of cell surface proteins by Rab11. *Trends Cell Biol* **24**, 407-415 (2014).
31. Eathiraj, S., Mishra, A., Prekeris, R. & Lambright, D.G. Structural basis for Rab11-mediated recruitment of FIP3 to recycling endosomes. *J Mol Biol* **364**, 121-135 (2006).
32. Miyawaki, A. & Tsien, R.Y. Monitoring protein conformations and interactions by fluorescence resonance energy transfer between mutants of green fluorescent protein. *Methods Enzymol* **327**, 472-500 (2000).
33. Pertz, O., Hodgson, L., Klemke, R.L. & Hahn, K.M. Spatiotemporal dynamics of RhoA activity in migrating cells. *Nature* **440**, 1069-1072 (2006).
34. Sakaguchi, A. et al. REI-1 Is a Guanine Nucleotide Exchange Factor Regulating RAB-11 Localization and Function in C. elegans Embryos. *Dev Cell* **35**, 211-221 (2015).
35. Gallo, L.I. et al. TBC1D9B functions as a GTPase-activating protein for Rab11a in polarized MDCK cells. *Mol Biol Cell* **25**, 3779-3797 (2014).
36. Chen, W., Feng, Y., Chen, D. & Wandinger-Ness, A. Rab11 is required for trans-golgi network-to-plasma membrane transport and a preferential target for GDP dissociation inhibitor. *Mol Biol Cell* **9**, 3241-3257 (1998).
37. Firestone, A.J. et al. Small-molecule inhibitors of the AAA+ ATPase motor cytoplasmic dynein. *Nature* **484**, 125-129 (2012).
38. Delevoye, C. et al. Recycling endosome tubule morphogenesis from sorting endosomes requires the kinesin motor KIF13A. *Cell Rep* **6**, 445-454 (2014).
39. Devereaux, K. et al. Regulation of mammalian autophagy by class II and III PI 3-kinases through PI3P synthesis. *PLoS One* **8**, e76405 (2013).
40. Gaidarov, I., Smith, M.E., Domin, J. & Keen, J.H. The class II phosphoinositide 3-kinase C2alpha is activated by clathrin and regulates clathrin-mediated membrane trafficking. *Mol Cell* **7**, 443-449 (2001).
41. Gulluni, F. et al. Mitotic Spindle Assembly and Genomic Stability in Breast Cancer Require PI3K-C2alpha Scaffolding Function. *Cancer Cell* **32**, 444-459 e447 (2017).
42. Marat, A.L. & Haucke, V. Phosphatidylinositol 3-phosphates-at the interface between cell signalling and membrane traffic. *EMBO J* **35**, 561-579 (2016).
43. Hoepfner, S. et al. Modulation of receptor recycling and degradation by the endosomal kinesin KIF16B. *Cell* **121**, 437-450 (2005).

Figure Legends

Fig. 1: The FRET biosensor AS-Rab11 specifically measures Rab11 nucleotide binding status.

a. Tridimensional representation of the genetically encoded fluorescence energy transfer (FRET) probe named AS-Rab11 (Activation Sensor Rab11) in its inactive (bound to GDP, left panel) or active conformation (bound to GTP, right panel). Yellow and light blue β-barrels represents a yellow- and cyan-emitting mutant of fluorescent proteins, respectively. Sea-green α-helix, black line and green β-barrels structures indicate Rab11-GTP binding domain (C-terminal region of FIP3), proteinase K sensitive linker domain and Rab11a protein, respectively. In this probe design, an increase of Rab11 GTP-loading promotes the binding of the C-terminal region of FIP3 to Rab11a, modifying the relative orientation of the two fluorophores and thereby increasing FRET signal (left and right panel).

b. Quantifications of FRET efficiency of AS-Rab11^{wt}, AS-Rab11 mutant forms, proteinase K treated AS-Rab11^{wt}; AS-Rab11^{wt} co-expressed with the indicated GEFs and their target GTPase (SH3BP5, RABEX-5, TIAM1, respectively); AS-Rab11^{wt} co-expressed with the indicated GAPs and their target GTPase (TBC1D9B, RN-3, ARHGAP15, respectively), and AS-Rab11^{wt} or AS-Rab11^{N206X} co-expressed with RabGDI (n=12 independent experiments; data represent mean ± SEM, *** $p< 0.005$, One-way ANOVA).

c. Representative FRET/CFP ratio images of AS-Rab11 biosensor in COS-7 cells (pseudocolor images represent FRET/CFP ratio intensity values). The upper and lower limits of the FRET/CFP ratio are shown on the left side bar (left panel). Magnification of FRET/CFP ratio images and AS-Rab11 localization in juxtanuclear (upper) and peripheral endocytic structures (lower) [right panel; pseudocolor images represent FRET/CFP ratio intensity values; grayscale image indicates emission of mcpVenus (AS-Rab11) after its direct excitation]. The scale bars represent 10 µm.

d. Representative line intensity profile of FRET sensitized (magenta) and CFP (cyan) signal detected in juxtanuclear (upper panel) and peripheral (lower panel) endocytic structures. The magenta and cyan image represent FRET sensitized and CFP signals, respectively. The scale bars represent 1 µm.

e. Scatter plot of sensitized FRET intensities as a function of CFP intensities in AS-Rab11 expressing cells (black and red dots represent the sensitized FRET and CFP intensity value of cytosolic and membrane-bound structures, respectively; regression line is in black) (upper panel) (n=4 independent experiments). Quantification of FRET/CFP ratio between cytosolic and endocytic structure labelled by AS-Rab11 (lower panel) (n=50 independent experiments; data represent mean ± SEM, *** $p< 0.005$, t-test).

f. Scatter plot of relative FRET efficiency as a function of distance from the nucleus for endocytic structures labelled by AS-Rab11 (upper panel) (n=4 independent experiments; black line represents mean ± SEM). Quantification of FRET/CFP ratio between juxtanuclear (ERC, from 0 to 3 µm from nucleus) and peripheral (PE, from 3 to 12 µm from the nucleus) endocytic structures labelled by AS-Rab11 (lower panel) (n=50 independent experiments; data represent mean ± SEM, *** $p < 0.005$, t-test).

Fig. 2: Juxtanuclear and peripheral localization of active Rab11 on distinct endosome populations.

a. Representative localization of active Rab11 on transferrin-positive endosomes. FRET/CFP ratio images (left panel, pseudocolor mode) of AS-Rab11 biosensor on endosomes labelled by fluorescent transferrin (left panel, gray scale). White line defines the region over which FRET/CFP ratio and fluorescent-transferrin signal were measured. The scale bar represents 1 μm.

Line intensity profile of FRET/CFP ratio (red line), labelled-transferrin (black line) and nuclei (blue line) (right upper panel)

Quantification in juxtanuclear (ERC, black bar) and peripheral (PE, red bar) endosomes of colocalization percentage (Pearson's correlation coefficient) between FRET/CFP signal and transferrin labelled endocytic structures (n=15 independent experiments; data represent mean ± SEM, t-test) (right lower panel)

b. Representative localization of active Rab11 on Rab4-positive endosomes. FRET/CFP ratio images (left panel, pseudocolor mode) of AS-Rab11 biosensor on endosomes labelled by mRFP-Rab4 (left panel, gray scale). White line defines the region over which FRET/CFP ratio and mRFP-Rab4 signal were measured. The scale bar represents 1 μm.

Line intensity profile of FRET/CFP ratio (red line), mRFP-Rab4 (black line) and nuclei (blue line) (right upper panel).

Quantification in juxtanuclear (ERC, black bar) and peripheral (PE, red bar) endosomes of colocalization percentage (Pearson's correlation coefficient) between FRET/CFP signal and Rab4 labelled endocytic structures (n=15 independent experiments; data represent mean ± SEM, t-test) (right lower panel).

c. Representative localization of active Rab11 on Rab5-positive endosomes. FRET/CFP ratio images (left panel, pseudocolor mode) of AS-Rab11 biosensor on endosomes labelled by mCherry-Rab5 (left panel, gray scale). White line defines the region over which FRET/CFP ratio and mCherry-Rab5 signal were measured. The scale bar represents 1 μm.

Line intensity profile of FRET/CFP ratio (red line), mCherry-Rab5 (black line) and nuclei (blue line) (right upper panel).

Quantification in juxtanuclear (ERC, black bar) and peripheral (PE, red bar) endosomes of colocalization percentage (Pearson's correlation coefficient) between FRET/CFP signal and Rab5

544 labelled endocytic structure (n=15 independent experiments; data represent mean ± SEM, *** p<
545 0.005, t-test) (right lower panel).

546 d. Representative localization of active Rab11 on PtdIns(3)*P*-positive endosomes. FRET/CFP
547 ratio images (left panel, pseudocolor mode) of AS-Rab11 biosensor on endosomes labelled by
548 mCherry-FYVE2X (left panel, gray scale). White line defines the region over which FRET/CFP
549 ratio and mCherry-FYVE2X signal were measured. The scale bar represents 1 μm.

550 Line intensity profile of FRET/CFP ratio (red line), mCherry-FYVE2X (black line) and nuclei (blue
551 line) (right upper panel)

552 Quantification in juxtanuclear (ERC, black bar) and peripheral (PE, red bar) endosomes of
553 colocalization percentage (Pearson's correlation coefficient) between FRET/CFP signal and
554 PtdIns(3)*P* labelled endocytic structures (n=15 independent experiments; data represent mean ±
555 SEM, *** p< 0.005, t-test) (right lower panel)

556

Fig. 3: Rab11 activation kinetics on PtdIns(3)P-positive endosomes.

a. Representative time-lapse series of cells co-expressing mCherry-Transferrin Receptor (TfR), mECFP-Rab11 and GFP- FYVE2X. White circles represent membrane bound structures. The scale bar represents 1 μm.

b. Representative time-lapse series of cells co-expressing AS-Rab11 and mCherry-FYVE2X. White circles represent membrane bound structures. The pseudocolor mode represents the FRET/CFP ratio; the gray scale indicates the emission of mcpVenus after its direct excitation. The scale bar represents 1 μm.

c. Quantification of FRET/CFP ratio (green line), mCherry-FYVE2X fluorescent emission (orange line) and AS-Rab11 mcpVenus emission (gray line) as a function of time in 28 individual vesicle tracks directed towards the ERC. The time point of detachment from early endosomes was recorded and used to shift the time courses so that all 28 detachment events were synchronized at the chosen time point of 0 s. The normalized FYVE2X is shown on primary vertical axis. The normalized value of FRET/CFP ratio is shown on secondary vertical axis (right)(n=4 independent experiments).

d. Representative time-lapse series of long range transport of active Rab11 vesicle towards the ERC. Gray scale represents mcpVenus fluorescence emission intensities before and after bleaching (left panel, the scale bar represents 5 μm). Magnification of juxtanuclear region and time-projection (right panel, the scale bar represents 1 μm). Pseudocolor mode represents FRET/CFP ratio (n=10 independent experiments).

e. Frequency distribution of $Rab11^{+}$ vesicle displacement from the origin in cells expressing GFP-$Rab11^{S25N}$ (green line) or GFP-Rab11 treated with either vehicle (DMSO, black line), Nocodazole, a microtubule depolymerizing drug (red line) or the dynein inhibitor, CiliobrevinD (blue line) (n=4 independent experiments, *** $p< 0.005$, * $p< 0.05$, two-way ANOVA).

f. Quantification of Rab11 activation in the perinuclear area. Cells were treated with either vehicle (DMSO, black line) or Nocodazole (red line) (n=14 independent experiments; data represent mean ± SEM, ** $p< 0.01$, t-test).

g. Quantification of Rab11 activation in the perinuclear area. Cells were treated with either vehicle (DMSO, black line) or Ciliobrevin D (red line) (n=14 independent experiments; data represent mean ± SEM, ** $p< 0.01$, t-test).

h. Frequency distribution of linearity of movement of $Rab11^{+}$ vesicles in cells expressing GFP-$Rab11^{S25N}$ (green line) or GFP-Rab11 treated with either vehicle (DMSO, black line), Nocodazole (red line) or Ciliobrevin D (blue line) (n=4 independent experiments; data represent mean ± SEM, *** $p< 0.005$, two-way ANOVA).

i. Representative image of endocytosed transferrin localization in cells expressing GFP-$Rab11^{S25N}$ or GFP-Rab11 treated with either vehicle (DMSO), Nocodazole or Ciliobrevin D (n=4 independent experiments). The scale bar represents 10 μm.

j. Quantification of perinuclear localization of fluorescent transferrin in cells expressing GFP-$Rab11^{S25N}$ (green bar) or treated with either DMSO/scramble siRNA (DMSO, black bar), Rab11 siRNA 1 ($RAB11\text{-}KD_1$, gray bar), Rab11 siRNA 2 ($RAB11\text{-}KD_2$, light blue bar), Nocodazole (red bar) or the dynein inhibitor, Ciliobrevin D (blue bar) (n=12 independent experiments; data represent mean ± SEM, *** $p< 0.005$, One-way ANOVA).

Fig. 4: PI3K-C2α-dependent Rab11 activation on PtdIns(3)P-positive endosomes.

a. Quantification of PtdIns(3)*P* abundance in COS-7 cells treated with either DMSO/Scramble siRNA (Control, black bar), VPS34 inhibitor (VPS34-IN1, red bar) or PI3K-C2α siRNA (PI3KC2α-KD, blue bar) (n=15 independent experiments; data represent mean ± SEM, *** $p< 0.005$, * $p< 0.05$, One-way ANOVA).

b. Quantification of Rab11 activity in COS-7 cells treated with either DMSO/Scramble siRNA (Control, black bar), VPS34 inhibitor (VPS34-IN1, red bar) or PI3K-C2α siRNA (PI3KC2α-KD, blue bar). (n=12 independent experiments; data represent mean ± SEM, * $p< 0.05$, One-way ANOVA).

c. Representative time-lapse series of cells co-expressing mCherry-FYVE2X, GFP-PI3K-C2α and mECFP-Rab11 (gray scale). White circles represent membrane-bound structures (n=6 independent experiments). The scale bar represents 1 µm.

d. Representative image of cells co-expressing mCherry-FYVE2X, mECFP-Rab11 (gray scale) and GFP-PI3K-C2α (PI3K-C2α) or its mutant version GFP-PI3K-C2α-ΔClathrin (PI3K-C2α-ΔClath). White circles represent membrane bound structures (n=6 independent experiments). The scale bar represents 1 µm.

e. Quantification of the number of Rab11-associated fission events generated from mCherry-FYVE2X positive membranes. COS-7 cells expressing GFP-Rab11^{S25N} (green bar) or GFP-Rab11 treated with either DMSO/Scramble siRNA (Control, black bar), VPS34 inhibitor (VPS34-IN1, red bar), PI3K-C2α siRNA (PI3KC2α-KD, blue bar). (n=10 independent experiments; data represent mean ± SEM, * $p< 0.05$, One-way ANOVA).

f. Residence time of GFP-Rab11^{S25N} (green bars) or GFP-Rab11 structures on mCherry-FYVE2X-positive membranes (black, blue, red bars). GFP-Rab11 expressing cells were treated with either DMSO/Scramble siRNA (Control, black bar), VPS34 inhibitor (VPS34-IN1, red bar), PI3K-C2α siRNA (PI3KC2α-KD, blue bar). (n=10 independent experiments; data represent mean ± SEM, *** $p< 0.005$, ** $p< 0.01$, Two-way ANOVA).

g. Quantification of internal transferrin percentage in cells expressing GFP-Rab11^{S25N} (green bar) or GFP-Rab11 treated with either DMSO/Scramble siRNA (Control, black bar), VPS34 inhibitor (VPS34-IN1, red bar), PI3K-C2α siRNA (PI3KC2α-KD, blue bar). (n=12 independent experiments; data represent mean ± SEM, ** $p< 0.01$, *** $p< 0.005$, One-way ANOVA).

h. Quantification of perinuclear localization of fluorescent transferrin in cells expressing GFP-Rab11^{S25N} (green bar) or GFP-Rab11 treated with either DMSO/Scramble siRNA (Control, black bar), VPS34 inhibitor (VPS34-IN1, red bar), PI3K-C2α siRNA (PI3KC2α-KD, blue bar) (n=12 independent experiments; data represent mean ± SEM, *** p< 0.005, One-way ANOVA).

i. Quantification of perinuclear localization of fluorescent transferrin in cells expressing GFP-Rab11 treated with either DMSO/Scramble siRNA (Control, black bar), PI3K-C2α siRNA (PI3KC2α-KD, red bar), PI3K-C2α siRNA and PI3K-C2α^{wt} siRNA resistant (PI3KC2α-KD/ PI3KC2α^{wt}, blue bar), PI3K-C2α siRNA and PI3K-C2α^{R1251P} siRNA resistant (PI3KC2α-KD/ PI3KC2α^{1251}, green bar), PI3K-C2α siRNA and PI3K-C2α^{CIII} siRNA resistant (PI3KC2α-KD/ PI3KC2α^{CIII}, purple bar) (n=12 independent experiments; data represent mean ± SEM, *** p< 0.005, One-way ANOVA).

Fig. 5: The PtdIns(3)P phosphatase MTM1 is a Rab11 effector.

a. Affinity chromatography of Rab11-GTP effectors. Representative western blot of both Rab11-GDP and Rab11-GTPγS column eluate probed with anti-MTM1, anti-MTMR2, anti-MTMR4, anti-MTMR6, and anti-MTMR9 antibodies (n=5 independent experiments)(uncropped blots are shown in Supplementary Figure 8).

b. Pull-down of endogenous Rab11-GTP and MTM1 complex. Representative western blot of Rab11-GTP pull-down assay probed with anti-MTM1 antibody (n=5 independent experiments). Quantification of endogenous MTM1 (central panel) and Rab11-GTP (right panel) pulled-down by GST or GST-RBD11 probe (n=5 independent experiments, data represent mean ± SEM, ** $p< 0.01$, t-test))(uncropped blots are shown in Supplementary Figure 8).

c. In vitro assessment of the association between recombinant Rab11-GTP and MTM1. Representative western blot of recombinant Rab11 loaded with GDP or GTPγS and probed for MTM1 interaction. Quantification of recombinant MTM1 pulled-down by recombinant Rab11 loaded with GDP or GTPγS (n=4 independent experiments, data represent mean ± SEM, ** $p< 0.01$, t-test)(uncropped blots are shown in Supplementary Figure 8).

d. Quantification of PtdIns(3)*P* abundance in COS-7 cells treated with either Scramble siRNA (Control, black bar) or MTM1 siRNA (MTM1-KD, blue bar). (n=12 independent experiments; data represent mean ± SEM, ** $p< 0.01$, t-test).

e. Quantification of active Rab11 levels in COS-7 cells treated with either Scramble siRNA (Control, black bar), MTM1 siRNA (MTM1-KD, blue bar), MTM1 siRNA and PI3K-C2α siRNA (MTM1-KD/PI3K-C2α-KD, dotted blue bar), MTM1 siRNA and VPS34 inhibitor (MTM1-KD/VPS34-IN1, dashed blue bar), MTM1 siRNA in combination with PI3K-C2α siRNA and VPS34 inhibitor (MTM1-KD/PI3K-C2α-KD/VPS34-IN1, red bar). (n=12 independent experiments; data represent mean ± SEM, ** $p< 0.01$, One-way ANOVA).

f. Representative immunofluorescence of COS-7 cells, showing peripheral and perinuclear colocalization of MTM1 with Rab11. Peripheral (left) and perinuclear (right) magnification are shown in the bottom part of the panel (n=6 independent experiments). White arrows highlight colocalization. The scale bar represents 15 μm.

g. Representative time-lapse series of cells co-expressing mCherry-Transferrin receptor (TfR), mECFP-Rab11 (gray scale) and GFP-MTM1. White circles represent membrane-bound structures (n=6 independent experiments). The scale bar represents 1 μm.

h. Quantification of the number of Rab11-associated fission events generated from mCherry-FYVE2X-positive membranes. Cells expressing GFP-Rab11^{S25N} (green bar) or GFP-Rab11 treated with either DMSO/Scramble siRNA (Control, black bar), MTM1 siRNA (MTM1-KD, blue bar), MTM1 siRNA and PI3K-C2α siRNA (MTM1-KD/PI3K-C2α-KD, dotted blue bar), MTM1 siRNA and VPS34 inhibitor (MTM1-KD/VPS34-IN1, dashed blue bar), MTM1 siRNA in combination with PI3K-C2α siRNA and VPS34 inhibitor (MTM1-KD/PI3K-C2α-KD/VPS34-IN1, red bar) (n=12 independent experiments; data represent mean ± SEM, ** $p< 0.01$, * $p< 0.05$, One-way ANOVA).

i. Residence time of GFP-Rab11^{S25N} (green bars) or GFP-Rab11 structures on mCherry-FYVE2X-positive membranes (black, blue bars). Cells expressing GFP-Rab11 were treated with either Scramble siRNA (Control, black bar) or MTM1 siRNA (MTM1-KD, blue bar). (n=12 independent experiments; data represent mean ± SEM, *** $p< 0.005$, ** $p< 0.01$, Two-way ANOVA).

j. Quantification of internal transferrin percentage in COS-7 cells expressing GFP-Rab11^{S25N} (green bar) or GFP-Rab11 treated with either DMSO/Scramble siRNA (Control, black bar), MTM1 siRNA (MTM1-KD, blue bar), MTM1 siRNA and PI3K-C2α siRNA (MTM1-KD/PI3K-C2α-KD, dotted blue bar), MTM1 siRNA and VPS34 inhibitor (MTM1-KD/VPS34-IN1, dashed blue bar), MTM1 siRNA in combination with PI3K-C2α siRNA and VPS34 inhibitor (MTM1-KD/PI3K-C2α-KD/VPS34-IN1, red bar) (n=12 independent experiments; data represent mean ± SEM, *** $p< 0.005$, ** $p< 0.01$, * $p< 0.05$, One-way ANOVA).

k. Quantification of perinuclear localization of fluorescent transferrin in COS-7 cells expressing GFP-Rab11^{S25N} (green bar) or GFP-Rab11 treated with either DMSO/Scramble siRNA (Control, black bar), MTM1 siRNA (MTM1-KD, blue bar), MTM1 siRNA and PI3K-C2α siRNA (MTM1-KD/PI3K-C2α-KD, dotted blue bar), MTM1 siRNA and VPS34 inhibitor (MTM1-KD/VPS34-IN1, dashed blue bar), MTM1 siRNA in combination with PI3K-C2α siRNA and VPS34 inhibitor (MTM1-KD/PI3K-C2α-KD/VPS34-IN1, red bar) (n=12 independent experiments; data represent mean ± SEM, *** $p< 0.005$, ** $p< 0.01$, One-way ANOVA).

Fig. 6: Trafficking of recycling cargo from peripheral endosome to ERC requires Rab11 activation and PtdIns(3)P turnover.

On a peripheral PtdIns(3)*P* membrane a transient and local burst of PI3K-C2α-derived PtdIns(3)*P* triggers Rab11 activation (first and second panel from the lefts). Active Rab11 (Rab11-GTP) recruits MTM1, a PtdIns(3)*P* phosphatase, that catalyzes PtdIns(3)*P* hydrolysis (third panel from the left). PtdIns(3)*P* reduction allows vesicle fission and trafficking of cargo towards the ERC (rightmost panel).

Materials and Methods:

Antibodies

The following antibodies were used in this study: mouse-anti-PI3K-C2α (BD Biosciences 611046, western blotting (WB) 1:500), mouse-anti-Rab11 (BD Biosciences 610656, WB 1:1000), rabbit-anti-MTM1 (SIGMA HPA010008, WB 1:1000), mouse-anti-FLAG (SIGMA clone M2, WB 1:2000), mouse-anti-GFP (ABCAM ab127417, WB 1:1000), rabbit-anti-VPS34 (Novus Biologicals NB110-87320SS, WB 1:1000), mouse-anti-MTMR4 (Santa Cruz sc-373922, WB 1:500), mouse-anti-MTMR6 (ABCAM ab69875, WB 1:1000), mouse-anti-MTMR9 (Santa Cruz sc-514366, WB 1:1000), rabbit-anti-FIP2 (ABCAM ab76892, WB 1:1000), rabbit-anti-FIP4 (Biorbyt orb215321, WB 1:1000). Anti-mouse IgG (ab131368, WB 1:5000) Anti-Rabbit IgG (A0545 SIGMA, 1:5000). anti mouse/rabbit IgG Alexa fluor 488/568 (IF 1:1000).

SiRNA and plasmid transfection

All siRNAs used in this study were 21-, 23-, or 27-base oligonucleotides including 3′-dTdT overhangs. For silencing, the following siRNAs were used targeting the human isoform: PI3K-C2α 5'-GGCAAGATATGTTAGCTTT-3', MTM1 5'-GATGCAAGACCCAGCGTAA-3′. The scrambled control siRNA used throughout this study corresponded to the sequence 5'-ATGAGTTAGATGCGTTCTA-3'.

COS-7 cells were transfected with siRNA using Lipofectamin 2000 (Invitrogen) according to the manufacturer's protocol. To achieve optimal knockdown efficiency, two rounds of silencing were performed. Cells were transfected on day 1, expanded on day 2, seeded for the experiment on day 3, and the experiment was performed on day 4.

For transient overexpression of proteins in silenced cells, plasmids were transfected on day 4 12 h before analysis using Lipofectamin 2000 (Invitrogen). For transient overexpression of proteins in untreated cells, plasmids were transfected 12 h before analysis using Lipofectamin 2000 (Invitrogen).

Recombinant protein production

GST-Rab11a recombinant protein was generated by cloning Rab11a cdna in pGex vector. Protein expression was induced by addition of isopropyl β-D–thiogalactoside (IPTG, 0.1 mM) at room temperature for 6 hours.

Recombinant proteins (GST-Rab11a, GST-Rab5a, GST-Rab7a) were purified (elution 10 mM glutathione, PBS), dialyzed, frozen in liquid nitrogen, and stocked (50% glycerol in Tris-HCl 50 mM 5 mM MgCl2, 100 mM NaCl) at −80°C. His-Flag-tagged MTM1 was generated according to previously established protocol [25]. In brief, Flagged MTM1 was clone in Pqe vector and bacteria were grown in 2X-YT (1% Yeast extract, 221 1% bactotryptone, 2,5mM NaOH and 0.5% NaCl) enriched medium until mid-log phase. Induction was performed with 1mM IPTG at 16°C for 12 hr. Soluble protein fraction was purified, dyalized, and stocked (50% glycerol in Tris-HCl 50 mM 5 mM MgCl2, 100 mM NaCl, 0.5% Triton).

Plasmids

The biosensor was built in sequential cloning steps using monomeric version of fluorescent proteins (A206K mutation) to avoid signal artifacts during FRET quantitation caused by multimerization of biosensor molecules into limited diffusional space, such as in membrane and vesicular compartments. Rab11 binding domain (RBD11) was fused with RBD11-circularly permutated Venus (mcpVenus) at residue 195, while cyan fluorescent protein (mECFP)-Rab11a fusions were first constructed. Two repetition of a linker encoding for a 17-mer unstructured soluble and proteinase-K sensitive polypeptide (GSTSGSGKPGSGEGSTK) [44] was then cloned by PCR that allow to maximize the FRET change between the active and inactive state. To construct RBD11-cpVenus, polymerase chain reaction (PCR) was used to amplify amino-acids 649-756 of FIP3 using the primers: 5'–CTAGCTAGCATGGGCCTGCAGGAGTACCACA–3' and 5'–GCTCTAGAATGGGCACCCGCGACG–3', and pGEX- FIP3 RBD11 as a template [9]. mcpVenus was amplified using the primers: 5'–GGTAGTGGTGAATTCATGCTCGGAGCAGTCCTGA–3' and 5'–ATCCCCTCGAGAGCACGGGGCCGTCGCCGAT–3' using ICUE3 FRET probe[45] as a template. Both fragments were then digested, gel purified, and subcloned in PGEM 3tEasy vector (Promega). The resulting fragment contained, from the 5'-end: a NheI site, RBD11, a EcoRI site, a linker (GGSG), and mcpVenus. This was cloned. To construct mECFP-Rab11a, a construct encoding mECFP was amplified with the primers: 5'–AAGCGGCCGCATGGTGAGCAAGGGCGAGGAGCTG–3' and 5'–GGTGCCCATTCTAGAAGTTCCCACGGGGGTACCAGCCTTGTACAGCTCGT–3'. Rab11a was amplified with the primers: 5'–GCTCTAGAATGGGCACCCGCGACG–3' and 5'–GCGGATCCAATGCCTTAGATGTTCTGACAGCACTGC–3' using a Rab11a expression construct as a template. Both fragments were then digested gel purified and subcloned in PGEM 3tEasy vector (Promega). The resulting fragment contained, from the 5'-end: a NotI site, a mECFP, a linker (GTPVGT), XbaI site, Rab11a and a BamHI site. In the next step, the 3' end of RBD11-

mcpVenus was flanked with zero, one or two copies of a sequence encoding a 17-mer, (GSTSGSGKPGSGEGSTK) generated by polymerase chain reaction (PCR). For that purpose, seven annealed 5' phopsorilated oligos: 5'–TCGAGGGGAGGCAGC–3', 5'–GGCCGCTGCCTCCCC–3' and 5'-TCGAGGGGATCAACTTCAGGATCAGGAAAACCCGGCTCCGGCGAGGGATCAACTAAAAGC–3' and 5'–GGCCGCTTTTAGTTGATCCCTCGCCGGAGCCGGGTTTTCCTGATCCTGAAGTTGATCCCC–3' and 5'–TATATATATATATATACTCGAGGGATCAACTTCAGGATCAGGAAAACCCGGCTCCGGCGAGGG–3'and 5'–CCGGGCTTGCCGCTGCCGGAAGTAGAGCCTTTAGTTGATCCCTCGCCGGAGCCGGG–3' and 5'–TATATATATATGCGGCCGCTTTTAGTTGATCCTTCTCCTGATCCGGGCTTGCCGCTGCCG-3' that encode the linker sequence flanked at the 5' by a XhoI and at the 3' by a NotI restriction site were ligated and subcloned in PGEM 3tEasy vector (Promega). To assemble the biosensor all the subcloned fragments were digested with the single cutter enzyme inserted at 5' and 3'-end, gel purified and cloned in pcDNA3.1(-myc/His) vector (Invitrogen), thus originating the following fusion protein containing from the N-terminus RBD11-cpVenu-2x17-mer linker-mECFP-Rab11a. The constructs were fully sequenced to ensure fidelity of the PCR reactions. Constituvely active (AS-Rab11^{Q70L}), dominant negative (AS-Rab11^{S25N}), a second constitutive active form (AS-Rab11^{S20V}) , an RBD mutant (AS-Rab11$^{RBD\ mutant}$ in which the "RBD domain" of FIP3 carries a 3 aminoacids mutation abrogating binding of active Rab11)[31], a nucleotide free form (AS-Rab11^{N124I}) and a mutant lacking GDI interaction (AS-Rab11^{N206X}, in which Asn-206 was changed to a stop codon, eliminating Rab11 prenylation/GDI binding site) versions of this biosensor were then engineered by site directed mutagenesis (Quikchange kit, Stratagene) using the following primers: 5'-GATATGGGACACAGCAGGGCTAGAGCGATATCGAGC-3', 5'-GCTCGATATCGCTCTAGCCCTGCTGTGTCCCATATC-3' and 5'-GATTCTGGTGTTGGAAAGAATAATCTCCTGTCTCG-3', 5'-CGAGACAGGAGATTATTCTTTCCAACACCAGAATC-3' and 5'-GTTGTCCTTATTGGAGATGTTGGTGTTGGAAAGAGTA-3', 5'-TACTCTTTCCAACACCAACATCTCCAATAAGGACAAC-3' and 5'-CAACTTCCGCCTGCAGGACGCCGCCGCCAGGATCATCGTGGCCATCAT-3', 5'-ATGATGGCCACGATGATCCTGGCGGCGGCGTCCTGCAGGCGGAAGTTG-3' and 5'-GTTATCATGCTTGTGGGCATTAAGAGTGATCTACGTCATCTC-3', 5'-

GAGATGACGTAGATCACTCTTAATGCCCACAAGCATGATAAC-3' and 5'-ATGTTCCACCAACCACTGAATAAAAGCCAAAGGTGCAGTGCTG-3', 5'-CAGCACTGCACCTTTGGCTTTTATTCAGTGGTTGGTGGAACAT-3'. Red fluorescent tagged version of Rab5, Rab4, Rab11 and Rab7 was generated by PCR and cloned into pmRFP-c1 plasmid.

The plasmid encoding RabGDI and GST-Rab7 were kindly provided by Cecilia Bucci from University of Salento. To allow the expression in mammalian cells the DNA sequence ecoding RabGDI and flanked by EcoRI site at 5' –end and BamHI site at 3'-end was subcloned in pcDNA3.1(-myc/His) vector (Invitrogen). A FLAG tag (DYKDDDDK) was inserted by digestion of pcDNA3.1(-myc/His)-RabGDI with EcoRI followed by calf intestinal phosphatase (CIP) treatment and gel purification. The opened plasmid was ligated with a linker sequence encoding the FLAG epitope obtained by annealing two 5'phosphorylated oligos with the following sequence: 5'–AATTCATGGACTACAAAGACGATGACGACAAGC-3' and 5'–AATTGCTTGTCGTCATCGTCTTTGTAGTCCATG–3'. The plasmid encoding hSH3BP5 was kindly gifted by Ken Sato from University of Gunma. A FLAG- N-terminal tag was added by PCR and the product of this reaction was cloned in pcDNA3.1(-myc/His) vector, thus generating a FLAG-hSH3BP5. The plasmid encoding TBC1D9B was kindly provided by Gerard Apodaca from University of Pittsburgh. A FLAG- N-terminal tag was added by PCR and the product of this reaction was cloned in pcDNA3.1(-myc/His) vector, thus generating a FLAG-TBC1D9B. The plasmid encoding mCherry-FYVE(2X) (pCI-neo-mCh-2XFYVE) was kindly gift by Matteo Bonazzi from University of Montpellier. The plasmid encoding TIAM1 was kindly gifted by Giorgio Scita and Andrea Palamidessi from IFOM in Milan. The plasmid encoding Rabex-5 was kindly gifted by Sara Sigismund from IFOM in Milan. The plasmid encoding RN-3 was kindly gifted by Letizia Lanzetti from IRCC in Candiolo.

Fluorometry assay

$2*10^5$ HEK 293T cells were plated in a 6-well plate and transfected using Lipofectamine 2000 (Invitrogen) according to manufacturer's instructions. In experiments in which the biosensor was co-transfected with a negative or positive regulator, the biosensor/regulator DNA ratio was 1/4. The total amount of transfected DNA was kept to 500 ng. 36 hours post-transfection, cells were lysed in lysis buffer (50 mM Tris-HCl, pH 7.4, 10 mM MgCl2, 100 mM NaCl, 1% Tritorn X-100, proteinase inhibitors) and clarified lysate was placed in a fluorometer cuvette. The lysates were analyzed using a Fluoromax-4 Horiba fluorometer. The lysates were excited at 433 nm and an

emission scan was acquired from 450 to 550 nm. To normalize for biosensor concentration a second measurement was made by directly exciting YFP at 505 nm and measuring its emission at 525 nm.

Immunoprecipitation assay for interaction of AS-Rab11 with SH3BP5 or AS-Rab11 with TBC1D9B

HEK 293T cells growing in 10-cm dishes were transfected with DNA mixtures containing 10 µg of pcDNA3.1(-myc/His)-Flag- SH3BP5 or 10 µg of pcDNA3.1(-myc/His)-AS-Rab11 or both, using calcium phosphate method. 48 h after transfection, cultures were harvested and homogenized in 0.5 ml of lysis buffer (50 mM Tris-HCl, pH 7.4, 0.2 mM GDP, 10 mM $MgCl_2$, 100 mM NaCl, 1% Tritorn X-100, 50 mM sodium fluoride, 1 mM phenylmethylsulfonyl fluoride). Cytosol was obtained by centrifuging the lysates at 20,000g for 30 min at 4 °C and protein concentration was determined by Bradford method. 1 mg of cytosol was incubated with FLAG M2 antibody (SIGMA, S.Louis, Missouri, USA) or with 1 µg of anti-GFP antibody (ABCAM, Cambridge, UK) for 2 hours and incubated on a rotating rack for 1 hour at 4 °C with Protein-G sepharose beads (GE, Buckinghamshire, UK). Samples were collected by centrifugation and washed six-times with phosphate wash buffer (10 mM NaH_2Po_4, 137 mM NaCl, and 2.7 mM KCl). Bound FLAG-SH3BP5, FLAG-TBC1D9B or GFP-AS-Rab11 protein complexes were then eluted by adding Laemmli sample buffer. SDS-PAGE and western blotting followed standard procedures. Similar approach was employed for the RabGAP TBC1D9B using the following lysis buffer: 50 mM Tris-HCl, pH 7.4, 0.2 mM GTP, 10 mM $MgCl_2$, 100 mM NaCl, 1% Triton X-100, 50 mM sodium fluoride, 1 mM phenylmethylsulfonyl fluoride).

Immunoprecipitation assay for interaction of AS-Rab11 with GDI

HEK 293T cells growing in 10-cm dishes were transfected with DNA mixtures containing 10 µg of pcDNA3.1(-myc/His)-Flag-RabGDI or 10 µg of pcDNA3.1(-myc/His)-AS-Rab11 or both, using calcium phosphate method. 48 h after transfection, cultures were harvested and gently homogenized in 0.5 ml of lysis buffer (50 mM Tris-HCl, pH 7.4, 0.2 mM GDP, 10 mM $MgCl_2$, 50 mM sodium fluoride, 1 mM phenylmethylsulfonyl fluoride). Cytosol was obtained by centrifuging the lysates at 20,000g for 30 min at 4 °C and protein concentration was determined by Bradford method. 1 mg of cytsol was incubated with FLAG M2 antibody (SIGMA, S.Louis, Missouri, USA) or with 1 µg of anti-GFP antibody (ABCAM, Cambridge, UK) for 2 hours and incubated on a rotating rack for 1 hour at 4 °C with Protein-G sepharose beads (GE, Buckinghamshire, UK). Samples was collected by centrifugation and washed six-times with phosphate wash buffer (10 mM NaH_2Po_4, 137 mM NaCl, and 2.7 mM KCl). Bound FLAG-GDI or GFP-AS-Rab11 protein

complexes were then eluted by adding Laemmli sample buffer. SDS-PAGE and western blotting followed standard procedures.

Radiolabeling of intracellular nucleotides and identification of the nucleotide-bound forms of AS-Rab11.

HEK293T cells cultured in 6 well plate dishes and transfected for 48 h were radiolabeled for 4 h with ^{32}P (6.0 MBq per dish) in phosphate-free DMEM (Invitrogen, Cat. Number 11971025). The expression levels of AS-Rab11 proteins and mutant forms were assessed by immunoblot analysis with the anti-GFP antibody (ABCAM, Cambridge, UK). The labeled cells ($7x10^5$ cells) were lysed with 0.3 ml of an ice-cold solubilizing buffer consisting of 40 mM Tris–HCl (pH 7.5), 100 mM NaCl, 20 mM $MgCl_2$, 1 mM Na_3VO_4, 1 mM dithiothreitol, 1% (w/v) Triton X-100, and 2 μg/ml aprotinin and clarified. The precleared lysates were incubated with anti-GFP antibody-immobilized Protein G–Sepharose beads (GE Healthcare) at 4 C for 30 min. After extensive washing of the immunocomplexes, associated nucleotides were separated by thin layer chromatography and quantified with a Amersham Hyperfilm MP (GE Healthcare).

Guanine nucleotide exchange assay

HEK 293T cells growing in 10-cm dishes were transfected with DNA mixtures containing 10 μg of pEGFP-Rab11a or 10 μg of pcDNA3.1(-myc/His)-AS-Rab11, using calcium phosphate method. At 48 h after transfection, cultures were harvested and homogenized in 1 ml of lysis buffer (50 mM HEPES, pH 7.6, and 1% (v/v) Triton-x100, 100 mM NaCl, protease inhibitors). Cytosol was obtained by centrifuging the lysates at 20,000g for 20 min at 4 °C and protein concentration of clarified lysates was determined by Bradford method. 1 mg of protein was immunoprecipitated using 1 μg of anti-GFP antibody (ABCAM, Cambridge, UK) for 1 hours and incubated on a rotating rack for 1 hour at 4 °C with Protein-G sepharose beads (GE, Buckinghamshire, UK). Samples were collected by centrifugation and washed six-times with buffer A containing 50 mM HEPES, pH 7.6, 1 mM DTT and 20 mM EDTA and incubated for 20 min at 25 °C, to remove Mg^{2+} and nucleotide bound to the Rab11 GTPases. The treatments of the samples with buffer A were repeated three times more. To determine the GDP binding affinities to Rab11 GTPases, [3H]GDP at a specific activity of 6000 cpm/μM was incubated with the respective apo-GTPases at 25 °C for 1 h in buffer B containing 50 mM HEPES, pH 7.6, 100 mM NaCl, 2.5 mM $MgCl_2$ and 1 mM DTT. Samples were collected by centrifugation and washed six-times with buffer C containing 50 mM HEPES, pH 7.6, 100 mM NaCl, 10 mM $MgCl_2$ to stop the binding reaction, and the radionucleotides remaining bound to the Rab GTPases were quantified by scintillation counting. To

measure the GDP/GTP exchange from Rab11 GTPases, the immunoprecipitated apo-GTPases were first complexed with [3H]GDP or in buffer B. After 60 min a binding equilibrium was reached, the dissociation reactions were initiated by the addition of 500 μM GTPγS to the incubation mixtures. At the indicated time intervals, samples were collected by centrifugation and washed six-times with buffer C to stop the exchange reaction. The radionucleotides remaining bound to the Rab GTPases were quantified by scintillation counting.

Rab11-activity pull down assay

Cells were washed in ice-cold PBS and lysed in 1 ml of MLB buffer (25 mM HEPES [pH 7.5], 150 mM NaCl, 1% Igepal CA-630, 10% glycerol, 25 mM NAF, 10 mM MgCl2, 1 mM EDTA, 1mM sodium orthovanadate, and protease inhibitor cocktail). Supernatant was collected after 15 min centrifugation at 13,000 rpm. A total of 1 mg of protein extract was incubated with 30 μg of recombinant protein coupled with glutathione S-transferase agarose (GE, Buckinghamshire, UK). The reaction mixture was gently rocked for 1 hr at 4°C. Beads were washed four times with lysis buffer. Samples were resuspended in Laemmli buffer for SDS-PAGE and immunoblot analysis. Endogenous content of total Rab11 in cell lysates was measured by loading 50 μg of total extracts in a different gel followed by immunoblot and used to normalize measurements of active Rab11. For quantification analysis, pictures were taken ensuring that intensity was within the linear range and the Quantity One 1-D analysis software (Bio-Rad) was used.

Rab11-effectors pull-down assay

50 μg of GST-Rab11 and corresponding molar amount of GST recombinant proteins were coupled to with glutathione S-transferase agarose (GE, Buckinghamshire, UK) and gently rocked for 1 hr at 4°C. Samples were collected by centrifugation and washed six-times with buffer A containing 50 mM HEPES, pH 7.6, 1 mM DTT and 20 mM EDTA and incubated for 20 min at 25 °C, to remove Mg^{2+} and nucleotide bound to the Rab11 GTPases. The treatments of the samples with buffer A were repeated three more times. GDP or GTPγS was added at a final concentration of 2mM and incubated with the respective apo-GTPases at 25 °C for 1 h in buffer B containing 50 mM HEPES, pH 7.6, 100 mM NaCl, 2.5 mM $MgCl_2$ and 1 mM DTT. Samples were collected by centrifugation and washed six-times with buffer C containing 50 mM HEPES, pH 7.6, 100 mM NaCl, 10 mM $MgCl_2$ to stop the binding reaction. Proteins on beads were incubated with either 1 ml of cell lysate made from a confluent dish of COS-7 cells lysed in 1 ml of MLB buffer (25 mM HEPES [pH 7.5], 150 mM NaCl, 1% Igepal CA-630, 10% glycerol, 25 mM NAF, 10 mM MgCl2, 1 mM EDTA, 1mM sodium orthovanadate, and protease inhibitor cocktail), or with recombinant

purified protein diluted in GST-binding buffer (20 mM Tris-HCl [pH 7.4], 100 mM NaCl, 5 mM MgCl2, 0.5% Triton X-100, 5 mg/ml BSA). After 1 hr, beads were washed with MLB or GST-binding buffer and proteins solubilized by boiling in LDS sample buffer.

Transferrin recycling assay

2 * 10^5 COS-7 cells were plated in a 6-well plate. After 24 hours, cells were starved for two hours in serum-free DMEM containing 0.1% BSA at 37°C, 5% CO_2, and then, where required, pretreated with 0.1% DMSO as control or with Vps34-IN1 1 uM for 30 min. 20 ug/ml of of alexa Fluor 647- conjugated human Transferrin (Invitrogen) were added for 30 min. After 37°C PBS washing, DMEM containing 0.1% BSA at 37°C, 5% CO_2 was added at various length times. Cells were then washed twice with cold PBS and acid stripping solution (150 mM NaCl, 2 mM $CaCl_2$ and 25 mM CH_3COONa, pH 4.5) was added for 4 min. For FACS analysis cells were detached with PBS 0.5 mM EDTA and fixed in 4% paraformaldehyde for 10 min. After resuspension in PBS, fluorescence flow cytometry was performed using a FACScalibur instrument. 20,000 cells were collected for each sample. The MFI of the cell population was recorded for each time point. Data were normalized to the time 0 MFI. For immunofluorescence analysis, cells were fixed in 4% paraformaldehyde for 10 min and imaged by confocal microscopy.

Internal Transferrin quantitation

2* 10^5 COS-7 wild-type (or interfered) cells were plated in a 6-well plate. After 24 hours, cells were starved for two hours in serum-free DMEM containing 0.1% BSA at 37°C, 5% CO_2, and then, where required, pretreated with 0.001% DMSO as control or with Vps34-IN1 1 uM for 30 min. 20 ug/ml of alexa Fluor 647- conjugated human Transferrin (Invitrogen) were added for 30 minutes to allow continuous uptake and recycling of labelled ligands. Cells were then washed twice with cold PBS and acid stripping solution (150 mM NaCl, 2 mM $CaCl_2$ and 25 mM CH_3COONa, pH 4.5) was added for 4 min. Cells were detached with PBS 0.5 mM EDTA and fixed in 4% paraformaldehyde for 10 min. After resuspension in PBS, fluorescence flow cytometry was performed using a FACScalibur instrument. 20,000 cells were collected for each sample. The MFI of the cell population was recorded for each time point. Data were normalized to control MFI values. For immunofluorescence analysis, cells were fixed in 4% paraformaldehyde for 10 min and imaged by confocal microscopy.

Cell Imaging

Cells were grown on μ-Dish $^{35mm, high}$ imaging dishes (Ibidi). Imaging was performed in CO_2 independent medium, Dulbecco's modified Eagle's medium without fetal bovine serum (GIBCO). Time-lapse series were acquired at 37°C on an inverted confocal Leica SP8 microscope with AOBS, equipped with 40X O2/Oil immersion objective, NA 1.30. The temperature was controlled by a climate box covering the set up. Hyd detectors (Leica) allowed the simultaneous detection of mECFP and mcpVenus or/and mCherry/mRFP, respectively. Fluorescent dyes were imaged sequentially in frame-interlace mode to eliminate cross talk between the channels. mECFP was excited with a 458-nm laser line and imaged at 470–500-nm bandpass emission filters. mcpVenus was exited with the 514-nm Argon laser line and imaged through a 525-550-nm bandpass emission filter. mCherry/mRFP was excited with the 568-nm Helium Neon laser line and imaged through a 580-650-nm bandpass emission filter. Alexa 647 dye was excited with the 633 nm Helium Neon laser line and imaged through a 650-700-nm bandpass emission filter. Serial sections were acquired satisfying the Nyquist criteria for sampling and processed using Matlab (MathWorks, MA, USA) and ICY software (http://icy.bioimageanalysis.org). Signals were referred to as individual structures if they comprised of a continuous patch of intensity values 50 (in a range of 0–255). At least two sections per cell were counted, ensuring that peripheral and perinuclear structures were equally taken into account. mECFP was bleached 5–10 times (2 s/scan) with zoom (x 15) with 100% laser power of the 458 nm Argon laser line. At the beginning of each experiment the number of bleaching steps that were sufficient to bleach mECFP was assessed and was kept constant all through. Acquisition was performed at zoom (x 11), in a region of 26 μm in side. The ROI has been chosen in order to contain the photobleached ERC and the surrounding intracellular region, and over a sufficiently large and homogeneous region to be able to visualize moving vesicles towards it. Exposure times and readout were fixed as follows: 200–300 ms for each channel followed by a 60-ms readout delay for the experiment in Figures 3a-f, i, 4b-g), resulting in timelapse sequences of roughly one frames per second. The timelapse sequences of roughly one frame per 30 seconds was used in Figures 3g, h, Supplementary Fig. 4a, 5a, b, d. Images obtained were merged and exported as a single TIFF file.

Image/video processing and data analysis

Image processing and analysis for total FRET activation in the cell were carried out with the Matlab software (MathWorks, MA, USA) integrated with Image Processing and Bioformats Toolbox. Following Gaussian smoothing, the image was converted to binary through thresholding, then median filtering, morphological closing and holes filling were applied to eliminate noisy pixels and smooth the images. The final mask was obtained computing the distance transform of the

binary image and using it as the input for a Watershed transform, thus enabling to discriminate and separate different contiguous endosomes from one to another. The threshold mask was then applied to sensitized FRET and CFP images and background subtraction was performed according to previous published protocol [46]. Finally, FRET activity ratio was calculated by dividing the unsaturated sensitized FRET pixels by the CFP pixels[47, 48]. To measure the dependence of FRET ratio on the distance from the nucleus, endosomes present in each frame included in the threshold mask were binned according to the distance of their centroid from the nuclear membrane.

Video processing and analysis for particle tracking and vesicle intensity profile were carried out with ImageJ, ICY [49] and R studio. Following background subtraction and Gaussian smoothing the CFP, FRET sensitized, YFP and red fluorescence were treated to eliminate noisy pixels and smooth the images. The FRET ratio for each frame was computed by dividing FRET sensitized signal by CFP signal. The videos were then imported in ICY for spot detection and particle tracking procedure performed on the YFP signal [50]. Intensity profile for FRET ratio, YFP and FYVE2X were exported together with trajectory for each detected vesicle. Vesicle intensity profiles were then aligned in R studio according to their speed profile and direction. The vesicle mean FRET ratio was adjusted by substracting cytoplasmic mean FRET ratio.

MatLab code is fully available on GitHub.

Statistical analysis

For biochemichal, immunocytochemistry and microscopy-based experiments a minimum of three independent experiments (n) was performed and statistically significant estimates for each sample were obtained. For microscopy based quantification, cells were chosen arbitrarily according to the fluorescent signal in a separate channel, which was not used for quantification where it was possible. Values were presented as means ± SEM. *P* values were calculated using two-tailed Student's *t* test and one- or two-way ANOVA followed by Bonferroni's multiple comparison posttest (GraphPad Software). Statistical significance is indicated as follows: $*P < 0.05$, $**P < 0.01$, and $***P < 0.005$.

Methods references

44. Whitlow, M. et al. An improved linker for single-chain Fv with reduced aggregation and enhanced proteolytic stability. *Protein Eng* **6**, 989-995 (1993).
45. DiPilato, L.M. & Zhang, J. The role of membrane microdomains in shaping beta2-adrenergic receptor-mediated cAMP dynamics. *Mol Biosyst* **5**, 832-837 (2009).
46. Broussard, J.A., Rappaz, B., Webb, D.J. & Brown, C.M. Fluorescence resonance energy transfer microscopy as demonstrated by measuring the activation of the serine/threonine kinase Akt. *Nat Protoc* **8**, 265-281 (2013).
47. Kardash, E., Bandemer, J. & Raz, E. Imaging protein activity in live embryos using fluorescence resonance energy transfer biosensors. *Nat Protoc* **6**, 1835-1846 (2011).
48. Jares-Erijman, E.A. & Jovin, T.M. FRET imaging. *Nat Biotechnol* **21**, 1387-1395 (2003).
49. de Chaumont, F. et al. Icy: an open bioimage informatics platform for extended reproducible research. *Nat Methods* **9**, 690-696 (2012).
50. Chenouard, N., Bloch, I. & Olivo-Marin, J.C. Multiple Hypothesis Tracking for Cluttered Biological Image Sequences. *IEEE Trans Pattern Anal Mach Intell* (2013).

Figure 1

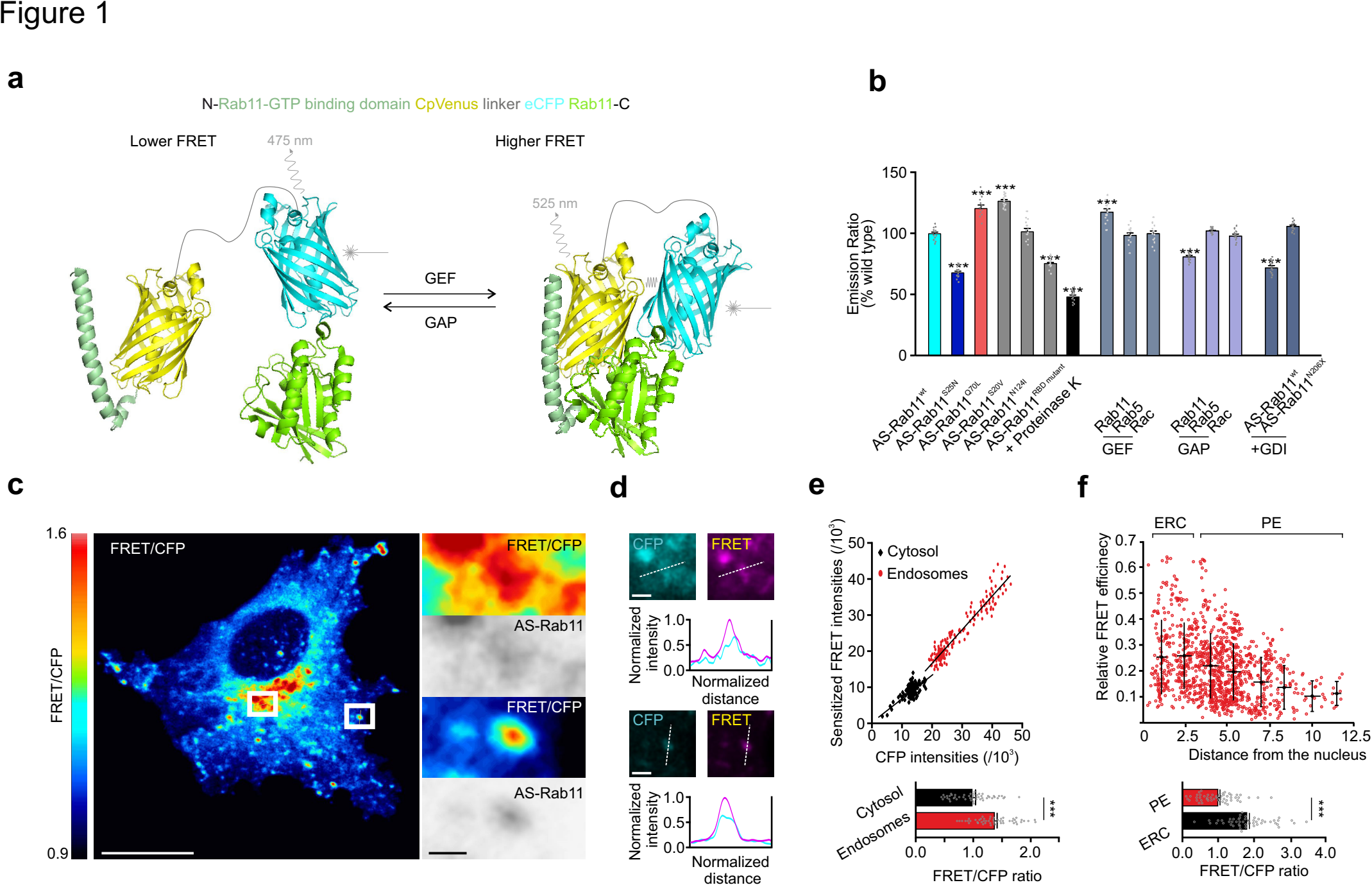
a
N-Rab11-GTP binding domain CpVenus linker eCFP Rab11-C
Lower FRET
475 nm
Higher FRET
525 nm
GEF
GAP
b
Emission Ratio (% wild type)
150
100
50
0
AS-Rab11wt
AS-Rab11S25N
AS-Rab11Q70L
AS-Rab11S20V
AS-Rab11N124I
AS-Rab11RBD mutant
+ Proteinase K
Rab11
Rab5
Rac
GEF
Rab11
Rab5
Rac
GAP
AS-Rab11wt
AS-Rab11N206X
+GDI
c
1.6
FRET/CFP
0.9
FRET/CFP
FRET/CFP
AS-Rab11
FRET/CFP
AS-Rab11
d
CFP
FRET
Normalized intensity
1.0
0.5
0.0
Normalized distance
CFP
FRET
Normalized intensity
1.0
0.5
0.0
Normalized distance
e
Sensitized FRET intensities (/10³)
50
40
30
20
10
0
Cytosol
Endosomes
0
10
20
30
40
50
CFP intensities (/10³)
Cytosol
Endosomes
***
0.0
1.0
2.0
FRET/CFP ratio
f
ERC
PE
Relative FRET efficinecy
0.7
0.6
0.5
0.4
0.3
0.2
0.1
0
2.5
5.0
7.5
10
12.5
Distance from the nucleus
PE
ERC
***
0.0
1.0
2.0
3.0
4.0
FRET/CFP ratio

Figure 2

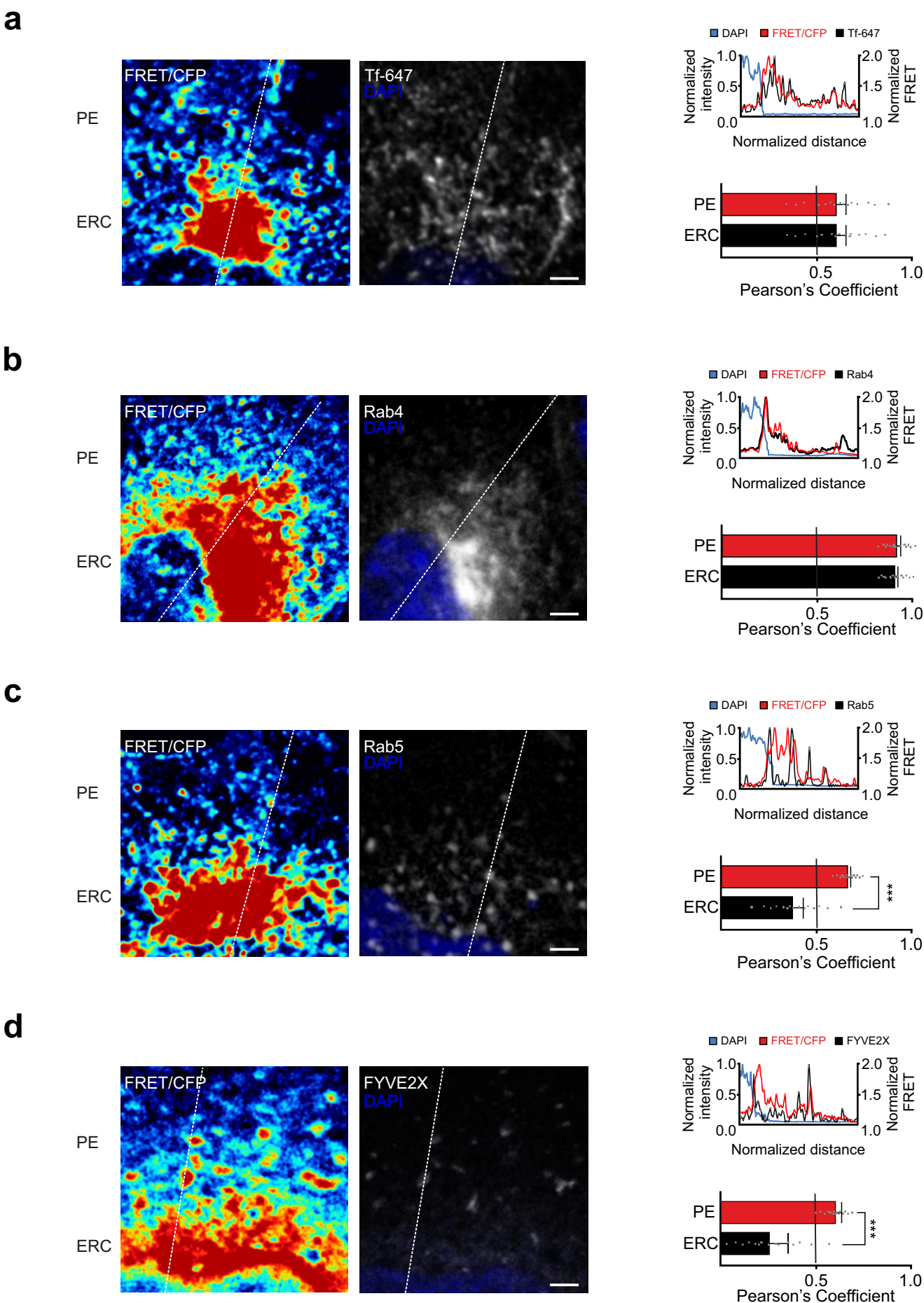
a
FRET/CFP
Tf-647
DAPI
PE
ERC
DAPI FRET/CFP Tf-647
Normalized intensity
Normalized FRET
Normalized distance
PE
ERC
Pearson's Coefficient
b
FRET/CFP
Rab4
DAPI
PE
ERC
DAPI FRET/CFP Rab4
Normalized intensity
Normalized FRET
Normalized distance
PE
ERC
Pearson's Coefficient
c
FRET/CFP
Rab5
DAPI
PE
ERC
DAPI FRET/CFP Rab5
Normalized intensity
Normalized FRET
Normalized distance
PE
ERC
***
Pearson's Coefficient
d
FRET/CFP
FYVE2X
DAPI
PE
ERC
DAPI FRET/CFP FYVE2X
Normalized intensity
Normalized FRET
Normalized distance
PE
ERC
***
Pearson's Coefficient

Figure 3

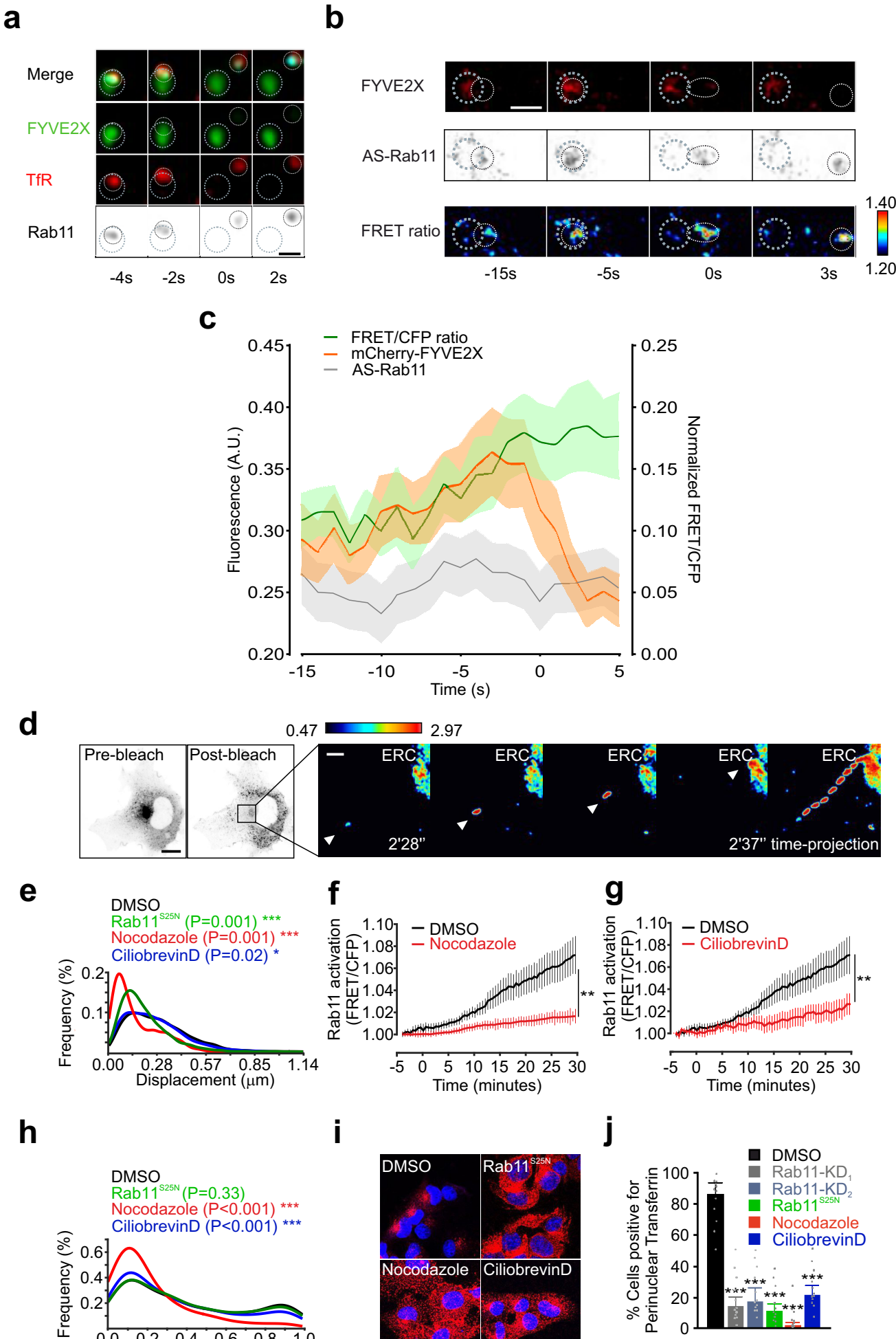
a
Merge
FYVE2X
TfR
Rab11
-4s
-2s
0s
2s
b
FYVE2X
AS-Rab11
FRET ratio
1.40
1.20
-15s
-5s
0s
3s
c
FRET/CFP ratio
mCherry-FYVE2X
AS-Rab11
Fluorescence (A.U.)
Normalized FRET/CFP
Time (s)
d
0.47
2.97
Pre-bleach
Post-bleach
ERC
2'28"
2'37" time-projection
e
DMSO
Rab11S25N (P=0.001) ***
Nocodazole (P=0.001) ***
CiliobrevinD (P=0.02) *
Frequency (%)
Displacement (μm)
f
DMSO
Nocodazole
Rab11 activation (FRET/CFP)
Time (minutes)
g
DMSO
CiliobrevinD
Rab11 activation (FRET/CFP)
Time (minutes)
h
DMSO
Rab11S25N (P=0.33)
Nocodazole (P<0.001) ***
CiliobrevinD (P<0.001) ***
Frequency (%)
Linear trajectory
i
DMSO
Rab11S25N
Nocodazole
CiliobrevinD
j
DMSO
Rab11-KD1
Rab11-KD2
Rab11S25N
Nocodazole
CiliobrevinD
% Cells positive for Perinuclear Transferrin

Figure 4

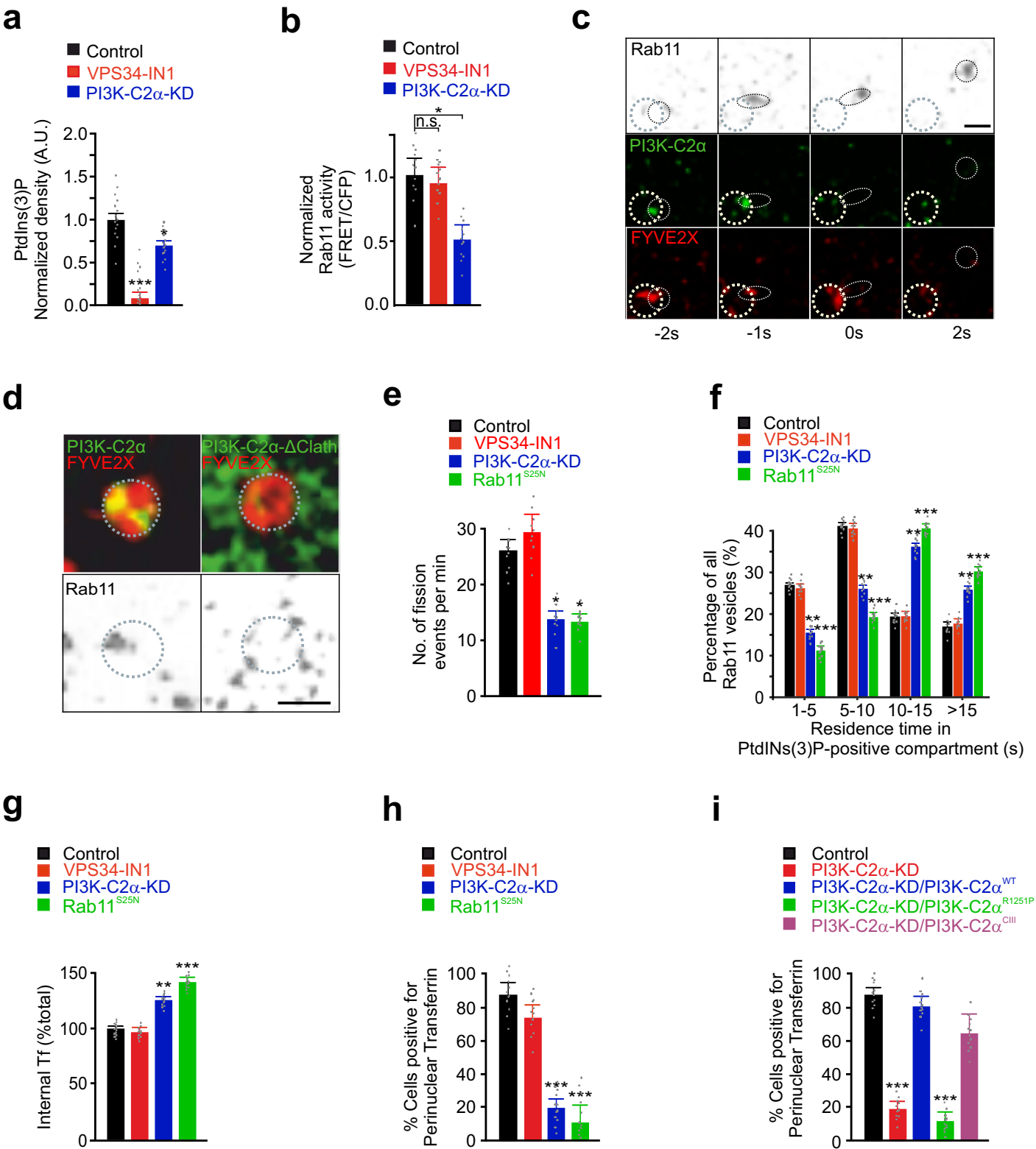
a
Control
VPS34-IN1
PI3K-C2α-KD
PtdIns(3)P Normalized density (A.U.)
2.0
1.5
1.0
0.5
0.0
***
*
b
Control
VPS34-IN1
PI3K-C2α-KD
n.s.
*
Normalized Rab11 activity (FRET/CFP)
1.0
0.5
0.0
c
Rab11
PI3K-C2α
FYVE2X
-2s
-1s
0s
2s
d
PI3K-C2α
FYVE2X
PI3K-C2α-ΔClath
FYVE2X
Rab11
e
Control
VPS34-IN1
PI3K-C2α-KD
Rab11S25N
No. of fission events per min
30
20
10
0
*
*
f
Control
VPS34-IN1
PI3K-C2α-KD
Rab11S25N
Percentage of all Rab11 vesicles (%)
40
30
20
10
0
1-5
5-10
10-15
>15
Residence time in PtdINs(3)P-positive compartment (s)
g
Control
VPS34-IN1
PI3K-C2α-KD
Rab11S25N
Internal Tf (%total)
150
100
50
0
**
***
h
Control
VPS34-IN1
PI3K-C2α-KD
Rab11S25N
% Cells positive for Perinuclear Transferrin
100
80
60
40
20
0
***
***
i
Control
PI3K-C2α-KD
PI3K-C2α-KD/PI3K-C2αWT
PI3K-C2α-KD/PI3K-C2αR1251P
PI3K-C2α-KD/PI3K-C2αCIII
% Cells positive for Perinuclear Transferrin
100
80
60
40
20
0
***
***

Figure 5

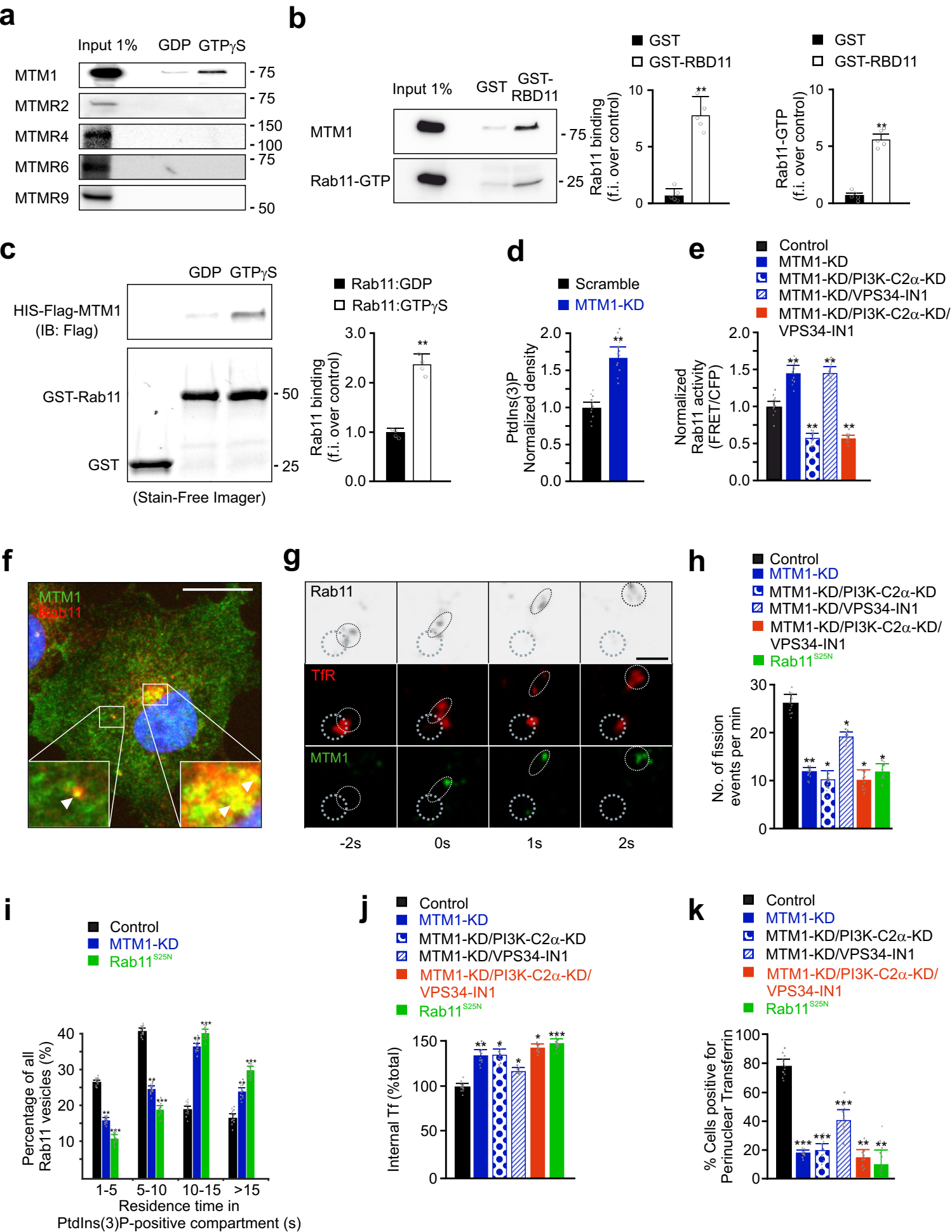
a
Input 1%
GDP
GTPγS
MTM1
MTMR2
MTMR4
MTMR6
MTMR9
75
75
150
100
75
50
b
Input 1%
GST
GST-RBD11
MTM1
Rab11-GTP
75
25
GST
GST-RBD11
Rab11 binding (f.i. over control)
Rab11-GTP (f.i. over control)
c
GDP
GTPγS
HIS-Flag-MTM1 (IB: Flag)
GST-Rab11
GST
50
25
(Stain-Free Imager)
Rab11:GDP
Rab11:GTPγS
Rab11 binding (f.i. over control)
d
Scramble
MTM1-KD
PtdIns(3)P Normalized density
e
Control
MTM1-KD
MTM1-KD/PI3K-C2α-KD
MTM1-KD/VPS34-IN1
MTM1-KD/PI3K-C2α-KD/ VPS34-IN1
Normalized Rab11 activity (FRET/CFP)
f
MTM1
Rab11
g
Rab11
TfR
MTM1
-2s
0s
1s
2s
h
Control
MTM1-KD
MTM1-KD/PI3K-C2α-KD
MTM1-KD/VPS34-IN1
MTM1-KD/PI3K-C2α-KD/ VPS34-IN1
Rab11S25N
No. of fission events per min
i
Control
MTM1-KD
Rab11S25N
Percentage of all Rab11 vesicles (%)
1-5
5-10
10-15
>15
Residence time in PtdIns(3)P-positive compartment (s)
j
Control
MTM1-KD
MTM1-KD/PI3K-C2α-KD
MTM1-KD/VPS34-IN1
MTM1-KD/PI3K-C2α-KD/ VPS34-IN1
Rab11S25N
Internal Tf (%total)
k
Control
MTM1-KD
MTM1-KD/PI3K-C2α-KD
MTM1-KD/VPS34-IN1
MTM1-KD/PI3K-C2α-KD/ VPS34-IN1
Rab11S25N
% Cells positive for Perinuclear Transferrin

Figure 6

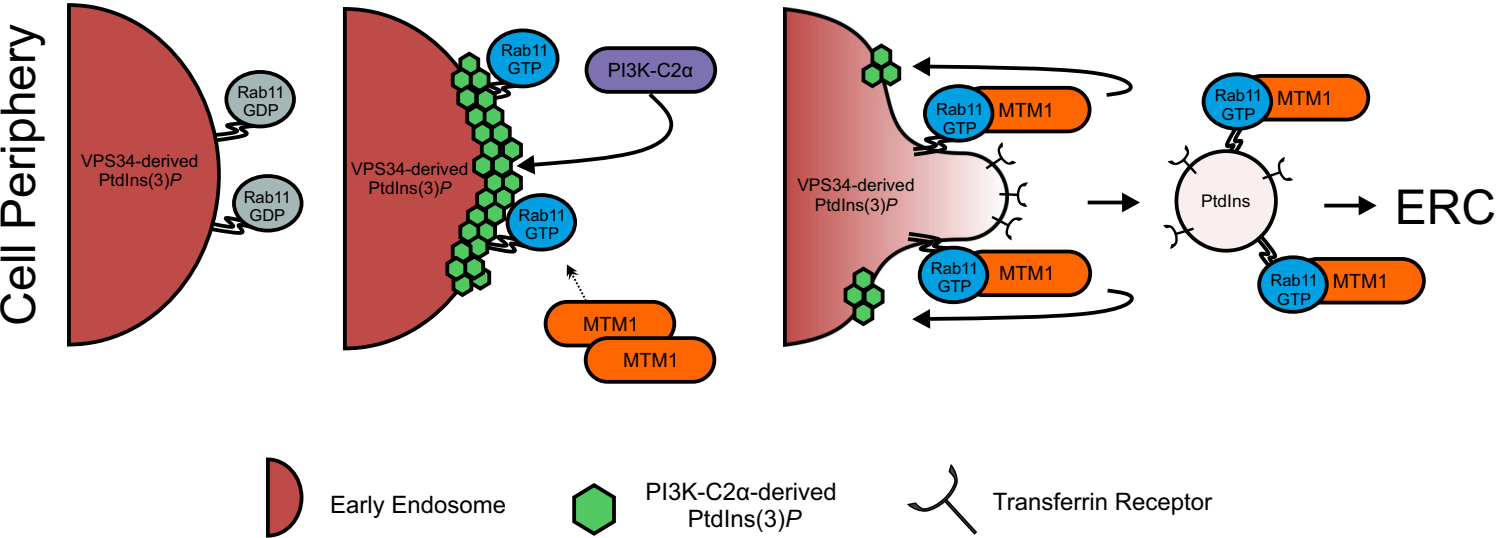
Cell Periphery
VPS34-derived PtdIns(3)P
Rab11 GDP
Rab11 GDP
VPS34-derived PtdIns(3)P
Rab11 GTP
PI3K-C2α
Rab11 GTP
MTM1
MTM1
VPS34-derived PtdIns(3)P
Rab11 GTP
MTM1
Rab11 GTP
MTM1
PtdIns
Rab11 GTP
MTM1
Rab11 GTP
MTM1
ERC
Early Endosome
PI3K-C2α-derived PtdIns(3)P
Transferrin Receptor

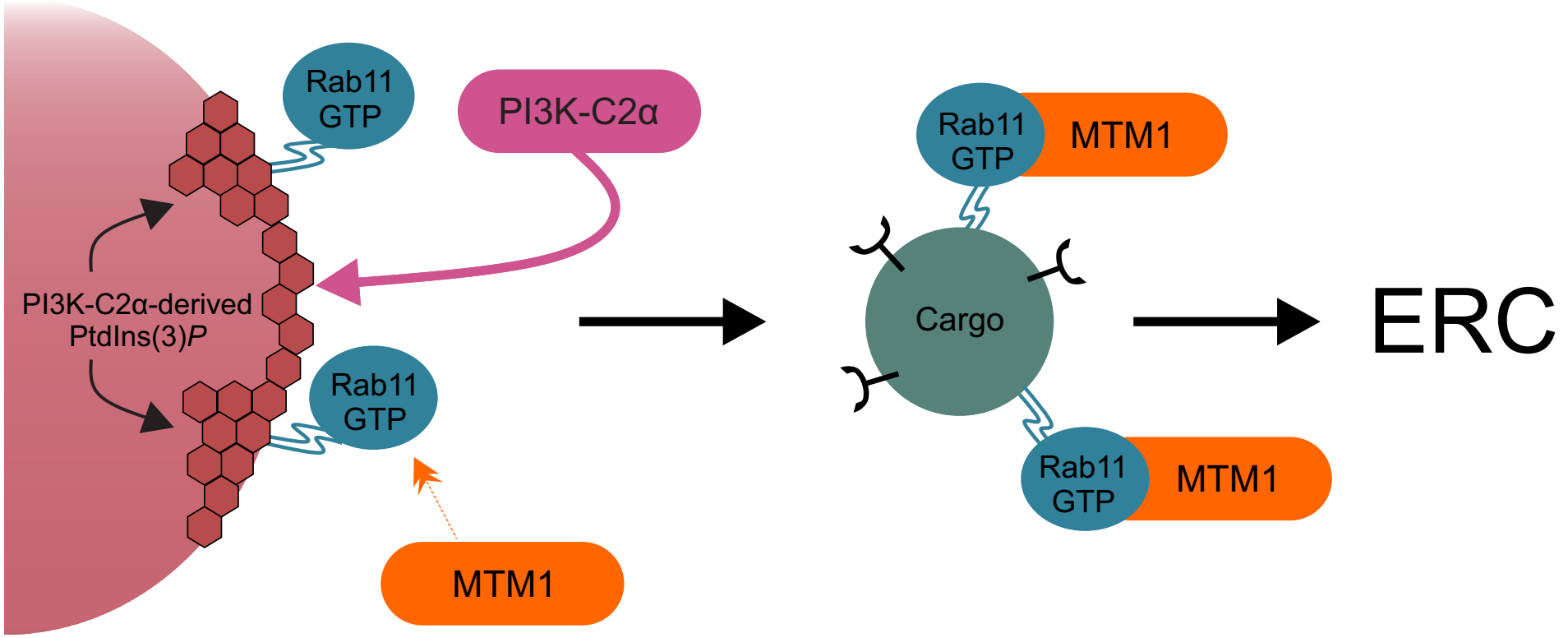
Rab11
GTP
PI3K-C2α
PI3K-C2α-derived
PtdIns(3)P
Rab11
GTP
MTM1
Rab11
GTP
MTM1
Cargo
Rab11
GTP
MTM1
ERC